Quasi-Biweekly Extensions of the Monsoon Winds and the Philippines Diurnal Cycle

Michael B. Natoli* and Eric D. Maloney†

Colorado State University Department of Atmospheric Science, Fort Collins, Colorado.

**Corresponding author*: Michael B. Natoli, mbnatoli@colostate.edu

†Current affiliation: Colorado State University Department of Atmospheric Science, Fort Collins, Colorado

ABSTRACT

The impact of quasi-biweekly variability in the monsoon southwesterly winds on the precipitation diurnal cycle in the Philippines is examined using CMORPH precipitation, ERA5 reanalysis, and outgoing longwave radiation (OLR) fields. Both a case study during the 2018 Propagation of Intraseasonal Tropical Oscillations (PISTON) field campaign and a 23-year composite analysis are used to understand the effect of the QBWO on the diurnal cycle. QBWO events in the west Pacific, identified with an extended EOF index, bring increases in moisture, cloudiness, and westerly winds to the Philippines. Such events are associated with significant variability in daily mean precipitation and the diurnal cycle. It is shown that the modulation of the diurnal cycle by the QBWO is remarkably similar to that by the boreal summer intraseasonal oscillation (BSISO). The diurnal cycle reaches a maximum amplitude on the western side of the Philippines on days with average to above average moisture, sufficient insolation, and weakly offshore prevailing wind. This occurs during the transition period from suppressed to active large-scale convection for both the QBWO and BSISO. Westerly monsoon surges associated with QBWO variability generally exhibit active precipitation over the South China Sea (SCS), but a depressed diurnal cycle. These results highlight that modes of large-scale convective variability in the tropics can have a similar impact on the diurnal cycle if they influence the local scale environmental background state similarly.

1. Introduction

The Philippines and its surrounding waters are prone to numerous types of atmospheric phenomena that make it highly vulnerable to climate risks (Yusef and Francisco 2009). During boreal summer (June-September, JJAS), the islands generally experience the southwest monsoon, which brings much of the region's annual precipitation (Moron et al. 2009; Matsumoto et al. 2020). While the agricultural sector relies on monsoon moisture, it can also bring devastating flooding (Cruz et al. 2013). The southwest monsoon is not always consistent throughout the season, rather, it is subject to numerous active and break cycles (Annamalai and Slingo 2001; Olaguera et al. 2020). These alternating periods of relatively enhanced activity and quiescence are modulated by several other modes of variability in the tropics, including the Madden-Julian Oscillation (MJO; or its boreal summer counterpart, the boreal summer intraseasonal oscillation (BSISO); Madden and Julian 1971; Krishnamurti et al. 1985; Lau and Chan 1986; Lawrence and Webster 2002), the quasi-biweekly oscillation (QBWO; Krishnamurti and Bhalme 1976; Krishnamurti and Ardanuy 1980; Chen and Chen 1995), equatorial waves (Ferrett et al. 2019), and tropical cyclones (Cayanan et al. 2011; Bagtasa 2019).

On a much shorter time scale than the aforementioned modes of precipitation variability is the diurnal cycle, which is of critical importance to the distribution of rainfall in the region (Bergemann et al. 2015; Zhu et al. 2017). The Maritime Continent (MC) region is home to complex topography, very warm sea surface temperatures (SSTs), and abundant heavy rainfall, all of which make for a complex diurnal cycle on each island (Ramage 1968). Islands generally observe an afternoon to evening peak in precipitation rates, instigated by land-sea breezes and mountain-valley breezes caused by differential heating between the land and surrounding waters (Houze et al. 1981; Qian 2008). Convection can become organized over large islands and then propagate offshore overnight

(Sakurai et al. 2005; Ichikawa and Yasunari 2006), assisted by convectively-generated gravity waves destabilizing the offshore environment (Mapes et al. 2003; Mori et al. 2004; Love et al. 2011; Hassim et al. 2016), and downslope mountain breezes, land breezes, and cold pools propagating storms offshore (Ohsawa et al. 2001; Ichikawa and Yasunari 2008; Wu et al. 2009; Fujita et al. 2011).

One of the most widely studied controls on the MC diurnal cycle is the MJO. Many studies have used various datasets to identify a preference for strong diurnal cycles to occur during the suppressed phase of the MJO (Sui and Lau 1992; Rauniyar and Walsh 2011; Oh et al. 2012). Others have more precisely illustrated a preference for the strongest diurnal cycles and offshore propagation in particular to occur in the transition from suppressed to active phase (Peatman et al. 2014; Natoli and Maloney 2019). In particular, recent field data from Sumatra has indicated a strong, propagating diurnal cycle as the MJO convective envelope approaches that then ceases once the westerly wind burst arrives (Wu et al. 2017, 2018).

While the BSISO has received less attention than its wintertime counterpart, evidence suggests that the above pattern of an enhanced diurnal cycle in the large-scale suppressed state or transition from suppressed to active states also holds true over the Asian summer monsoon region. Over the Philippines, the diurnal cycle appears to reach a maximum during the BSISO suppressed state (Ho et al. 2008; Park et al. 2011; Xu and Rutledge 2018; Xu et al. 2021), although the typical afternoon maximum is still present in the active state (Chudler et al. 2020). Recently, Natoli and Maloney (2019) examined the impact of the BSISO on the Philippine diurnal cycle in detail, and noted a maximum in the diurnal amplitude over land and coastal waters of the South China Sea (SCS) during the transition from suppressed to active BSISO state when the mid-tropospheric moisture begins to increase, but prior to the arrival of strong westerly monsoon winds.

A consensus on the mechanisms involved in this interaction remains out of reach. Some studies such as Peatman et al. (2014) have suggested that frictional moisture convergence associated with the Kelvin wave to the east of MJO convection (Gill 1980) contributes to the early increase in the diurnal cycle, although this mechanism is not relevant in off-equatorial regions. Lu et al. (2019) more recently indicated that moisture convergence is indeed an important factor to the diurnal cycle development, but it is the diurnal scale wind (i.e. land-sea breeze) converging the MJO scale moisture that is most important, consistent with Natoli and Maloney (2019).

The relationship between the diurnal cycle and other modes of tropical variability has also been recently getting more attention. Notably, Sakaeda et al. (2020) took a thorough look at the impact of various equatorial wave modes on the MC diurnal cycle during boreal winter, noting important differences in behavior between various wave modes and individual islands. They also distinguished diurnal cycle behavior within an individual island related to the position relative to the wind (leeward vs. windward), and aspect of topography. Specifically, the diurnal cycle was found to be enhanced on the leeward side of MC islands for the MJO and n=1 equatorial Rossby (R1) waves, consistent with Virts et al. (2013) and Qian (2020). Leeward enhancement of the diurnal cycle has also been identified in the Philippines (Natoli and Maloney 2019; Riley Dellaripa et al. 2020).

As the BSISO (or MJO) can be manifest as active and break periods in the southwesterly monsoon over the SCS (Chen and Chen 1995; Bagtasa 2020), other modes of variability that similarly modulate the monsoonal flow over the Philippines may also impact the diurnal cycle. Differences in how another mode impacts the monsoon background may be insightful in ascertaining the primary controls on the diurnal cycle itself. Variance in boreal summer outgoing longwave radiation (OLR) shows the global maximum of the quasi-biweekly (10-20 day) time scale occurring in the South China and Philippine Seas (Qian et al. 2019). The importance of this mode in determining monsoon activity has been a subject of research for decades, first identified in the Indian monsoon region (Krishnamurti and Bhalme 1976; Krishnamurti and Ardanuy 1980; Chen and Chen 1993), before being later explored in the west Pacific and east Asian monsoon regions (Chen and Chen 1995; Chen et al. 2000).

This mode has often been described as the quasi-biweekly oscillation (QBWO), consisting of a northwestward propagating region of anomalous moisture, convection, westerly winds, and cyclonic vorticity (Kikuchi and Wang 2009; Tao et al. 2009; Li et al. 2020). Disturbances tend to emerge in the equatorial western Pacific and propagate through the Philippine Sea, South China Sea, and into Asia, frequently impacting the Philippines (Chen and Sui 2010; Yan et al. 2019). Many of these studies refer to the QBWO in a statistical rather than physical sense, but there is evidence that multiple phenomena can contribute to quasi-biweekly variability, and thus project onto various QBWO indices. The westward propagating mode ubiquitous in the west Pacific is often traced to a moist, R1 wave (Matsuno 1966) that is modified by the monsoon background state (Chatterjee and Goswami 2004). In addition to its modulation of the monsoon onset and persistence (Qian et al. 2019), the QBWO has noteworthy impacts on tropical cyclones (Zhou et al. 2018; Han et al. 2020), extreme rainfall (Liu et al. 2014), and heatwaves in China (Chen et al. 2016; Gao et al. 2018).

Research on the relationship between the QBWO and the diurnal cycle remains sparse. The present study aims to explore this relationship in detail, and determine how well the ideas presented for the MJO/BSISO-diurnal cycle interaction apply to a different mode of tropical convective variability that has received less attention. Specifically, if another large-scale feature impacts the environmental background conditions (e.g. lower tropospheric wind and mid-tropospheric moisture) in a similar way to the BSISO, will the diurnal cycle respond similarly? The first goal is to describe west Pacific variability on the 10-20 day timescale and its importance to the Philippine archipelago. This includes examination of prominent variability on this timescale that occurred during a recent major field program (Sobel et al. 2021). Second, an index for the QBWO will be described that can be used to composite precipitation and other variables. Third, we aim to establish the impact of the quasi-biweekly mode on the diurnal cycle of the Philippines and its offshore propagation. The final goal is to compare and contrast the QBWO-diurnal cycle relationship with the MJO-diurnal cycle relationship over the Philippines to help reveal important controls on diurnal convection and the mechanisms involved.

The next section will describe the data and methods used, followed by a description of the QBWO index used in this study. In Section 3, results will be discussed, starting with a case study during the 2018 PISTON field campaign, then leading into a composite analysis for the period 1998-2020 from the large scale to the island scale. Section 4 includes a discussion of the mechanisms and a comparison with the BSISO, with a summary and major conclusions outlined in section 5.

2. Data and Methods

a. Data Description

This study employs several datasets to analyze quasi-biweekly variability in the monsoon and the diurnal cycle of precipitation. First, precipitation data comes from version one of the Climate Prediction Center (CPC) Morphing Technique (CMORPH; Joyce et al. 2004; Xie et al. 2017). The data is available as 30-minute total precipitation accumulation estimates at 8-km spatial resolution, covering 60°S-60°N. The CMORPH method takes precipitation rate estimates from passive microwave satellite retrievals and then uses cloud-motion vectors derived from infrared satellites to morph and interpolate through space and time to other passive microwave estimates. Thus, infrared information is only used to predict storm motion, and is not directly used to estimate precipitation rates. These initial estimates are bias-corrected against gauge data and the Global Precipitation Climatology Project (Adler et al. 2003) to yield the final product. Other studies have shown that this bias-corrected CMORPH technique removes most of the bias over land in warm climates (as in this study), and performs favorably when compared with the commonly used TRMM 3B42 precipitation dataset (Xie et al. 2017). CMORPH also demonstrates similar skill compared against the IMERG product (Huffman et al. 2015; Sahlu et al. 2016). The same analysis described below was performed for IMERG during the available period of 2000-2020 and the results remain robust.

Complementing the precipitation data, the 5th Generation Reanalysis from the European Centre for Medium-Range Weather Forecasting (ERA5; Hersbach et al. 2020; Copernicus Climate Change Service (C3S) 2017) is used for JJAS, 1998-2020. Variables analyzed here include total column water vapor, surface downwelling shortwave radiation, and 850-hPa wind. Each of these fields are considered at 1-hour temporal resolution and 0.25° spatial resolution. In this study, the purpose of the ERA5 data is to contextualize the precipitation results and elucidate potential mechanisms. Additional variables were examined on numerous pressure levels through the troposphere, but these did not add further insight and are not included in this discussion.

In addition, interpolated outgoing longwave radiation (OLR) data from the Advanced Very High Resolution Radiometer (AVHRR) is analyzed at daily temporal and 2.5° spatial resolution for JJAS, 1979-2020 (Liebmann and Smith 1996). OLR is used to calculate the QBWO index used in this study, as well as track large-scale convection associated with it. Zonal wind data from balloon soundings in the 2018 PISTON field campaign are also used at 3-hourly resolution from the R/V Thomas G. Thompson and 12-hourly resolution from Yap Island (Sobel et al. 2021). Processing and quality control for sounding data follows Ciesielski et al. (2014). These locations relative to the Philippines are shown in Figure 1. Lastly, topographic data from the National Oceanic and Atmospheric Administration's (NOAA) ETOPO2 dataset are incorporated to provide geographic context for the results (National Geophysical Data Center 2006). The BSISO index used in this study for comparison to the QBWO results is that by Lee et al. (2013), which we used in Natoli and Maloney (2019). The QBWO index used will be described below.

b. Methods

The compositing method in this study follows that of Natoli and Maloney (2019), in which a single composite diurnal cycle is created for CMORPH precipitation for all days in JJAS in the analysis period, defined here as the boreal summer composite diurnal cycle. In addition, separate composite diurnal cycles are created by averaging measurements from only days in that period in which an index of intraseasonal variability (e.g. QBWO or BSISO) was considered active and in a certain phase (one of eight). An anomaly in this study refers to the difference between the composite of interest and the JJAS mean. Statistical significance of the precipitation results also follows Natoli and Maloney (2019) using a bootstrapping method, where the composite diurnal cycle in an ISO phase was compared against 1000 composite diurnal cycles taken from random days in the study period, with a Poisson distribution used to account for the fact that ISO active days tend to come in non-independent groups of several days. More details can be found in Natoli and Maloney (2019).

This study also calculates power spectra for a few different time series. This is done by calculating the spectrum for each season individually (e.g. JJAS 1998, 1999, etc.) after applying a Hanning window to reduce the Gibbs phenomenon. Then, spectra are averaged from all years to increase degrees of freedom, only considering the relevant season (boreal summer). The theoretical red noise spectra follow equation 5 of Gilman et al. (1963), which provides an estimate for how a power spectrum of a pure red noise process with the same autocorrelation as the time series of interest would appear. An F-test is employed to determine if the calculated power spectrum is significantly different from its corresponding theoretical red noise spectrum. OLR data is also bandpass filtered to 10-20 days in this study to prepare the data for calculation of the QBWO index, and highlight variability on relevant timescales for analysis of the 2018 PISTON period. This is done by applying a Lanczos filter with 93 weights to detrended OLR data at each grid point (Duchon 1979).

c. QBWO Index

An index was created to track the QBWO in the west Pacific and facilitate analysis of its relationship to the Philippine diurnal cycle. Many prior studies have created indices for this features, but a consensus has yet to emerge on the best method (Kikuchi and Wang 2009; Han et al. 2020; Yan et al. 2019; Qian et al. 2019). The timescale studied for the QBWO also differs in the literature, but most include the 10-20 day period, with some extending to 25 or 30 days on the low frequency end, and others extending to 5 or 7 days on the high frequency end. Here, we attempt to exclude both timescales more characteristic of synoptic scale variability (5-10 days), as well as the longer time scales approaching the BSISO mode (20-30 days), and select a band of 10-20 days upon which to base our index. This timescale was found to display consistent westward propagating activity in the region of interest that also resembles the QBWO behavior documented in previous studies (Chatterjee and Goswami 2004; Chen and Sui 2010; Li et al. 2020). Additionally, the 10-20 day band well-captures the spectral peak in lower tropospheric wind variability near the Philippines.

Figure 2a shows the power spectrum calculated from 850-mb ERA5 zonal wind averaged over northern Luzon (box L in Fig. 1) during JJAS 1998-2020. A statistically significant spectral peak is identified around 10-15 days. This peak is robust across averaging domains that vary in both size and shape surrounding the Philippine archipelago. Thus, the 10-20 day band encompasses the spectral peak in the region of interest, produces the structure outlined in previous studies, and excludes other time scales that may muddy results (Chen and Sui 2010; Yan et al. 2019). Fig. 2b shows the same for Mindanao over box M, indicating a weaker but noticeable peak in the 10-15 day band that does not reach statistical significance.

The architecture of our index is most similar to that of Qian et al. (2019), only differing in temporal and spatial domain, and filtering time scale that improve variance explained by the index. EEOFs are calculated from the 10-20 day OLR anomalies inside the domain of 0-35N, and 115-165W for JJAS 1979-2020, with information included at lags 0, 2, and 4 days prior. The spatial patterns associated with the two leading modes of variability in 10-20 day OLR are shown in Fig. 3, which explain 16.67% and 16.31% of the variance respectively. They are well separated from the other EOFs (not shown) and represent a propagating wave-like signal based on a lag correlation analysis of their unfiltered principal components (described below in more detail) that maximizes at 3-4 days. The coherence squared between the two PCs averaged inside the 10-20 day band is 0.81. The patterns are presented in Figure 3 such that time progresses going downward, and the pattern at lag 4 of EEOF 2 is roughly equivalent to the lag 0 pattern of EEOF 1. Thus, the time progression continues through EEOF 1 first, and then through the lags of EEOF 2. The spatial patterns shown here were not highly sensitive to choice of domain, filtering timescale (as long as 10-20 day band was included), lag timescale, and months analyzed. Other periods in addition to JJAS were considered, but precipitation patterns over the northern Philippines appear somewhat distinct in May or October (not shown), which motivated the choice for the shorter season.

To calculate the principal component (PC) time series, the *unfiltered* OLR anomalies (with the seasonal cycle removed) are projected back onto the EEOF patterns in Fig. 3. Since unfiltered OLR anomalies make up the PCs, it must be assured that they still capture the 10-20 day timescale well, as we do allow for other time scales to project on the index. Spectra for both PC1 and PC2 (Fig. 3d, h) show strong, statistically significant peaks in spectral power on 10-20 day timescales. While there is some bleeding to both higher and lower frequencies, no distinct peak can be seen elsewhere in the spectrum, which provides confidence that this index is picking up westward propagating signals that oscillate on roughly 10-20 day time scales.

The use of an EEOF index also allows for more direct comparison to MJO or BSISO studies that employ the commonly-used RMM index for the MJO (Wheeler and Hendon 2004), or the Lee et al. (2013) index for the BSISO. We can split the phase space into 8 phases according to the sign and magnitude of the corresponding PC time series for each day. Since the choices of the sign of each PC and which PC to make the x-axis or y-axis in the phase space are arbitrary, we defined them in this study such that the "active" phases for the Philippines most closely correspond to the "active" phases of the Lee et al. (2013) index for the BSISO. In other words, phases 2-4 generally correspond to suppressed convection and low-level easterly winds over Luzon for both indices, while phases 6-8 generally indicate enhanced convection and strong westerlies. This allows for the direct comparison of the precipitation behavior and background conditions over the Philippines later in this manuscript.

It is important to verify that our QBWO index is reasonably independent from the Lee et al. (2013) BSISO index before composites for each are directly compared in the subsequent sections. Fig. 4 shows the number of days in a certain Lee et al. (2013) BSISO phase classified by each QBWO phase. The vast majority (between 71 and 80%) of active QBWO days have an inactive BSISO, and there is no preference for a day to be classified as the same numbered phase in each index. This percentage is consistent with BSISO activity across the entire study period, as the index is inactive about 75% of the JJAS days between 1998 and 2020. Anti-correlation between QBWO and BSISO activity has also been found on interannual timescales (Yang et al. 2008). The third and fourth multivariate EOF identified by Lee et al. (2013), which are by definition independent from the first two EOFs which make up the BSISO index, have been shown to capture some QBWO variability (Qian et al. 2019). Thus, the QBWO index appears to be randomly selecting from BSISO activity, and we can assume that they are independent.

3. Results

a. 2018 PISTON Case Study

The operational period of the 2018 PISTON field campaign (14 August - 14 October 2018) is used as a case study to assess this index and 10-20 day variability for a specific time period, before leading into a more general composite analysis in the next subsection. This time period was selected because prominent 10-20 day variability was apparent in raw data during a major field campaign (Sobel et al. 2021). One of the original goals of the 2018-19 PISTON project was to sample lower frequency intraseasonal oscillations, like the BSISO. However, the 2018 leg of the experiment witnessed minimal BSISO activity during the two month long cruise, only sampling a suppressed phase of an MJO-like disturbance in early October. While exploration of the tropical QBWO was not an original goal, the noteworthy variability observed on this timescale described below presents an opportunity to learn more about this feature (Sobel et al. 2021).

Figure 5 shows a time-height diagram of zonal wind observations from radiosondes released during PISTON. The top panel shows 12-hourly soundings released from the Yap island, while the bottom shows the 3-hourly soundings released aboard the R/V Thomas G. Thompson, with white space when the ship was in port or in transit (see Fig. 1 for locations). Both locations in the west Pacific observed significant variability in zonal wind on 10-20 day timescales. Roughly every two or three weeks, the region experienced surges of fairly strong westerly winds in the low levels, extending through much of the troposphere and lasting about 7-10 days. Westerly winds tapped into deep monsoonal flow bringing increased moisture and increased mesoscale convective system activity (Chudler and Rutledge 2021; Sobel et al. 2021). Such monsoon surges were often caused by and/or enhanced by tropical cyclones (TCs) passing northeast of the study domain, similar to events described in Cayanan et al. (2011) and Bagtasa (2017). These were interspersed with tranquil periods of weak trade easterlies. The identification of enhanced QBWO activity during the 2018 boreal summer season is consistent with prior work suggesting a preference for such activity during El Niño years (the late summer of 2018 featured a strengthening El Niño event) and during periods of decreased BSISO activity (Yang et al. 2008; Yan et al. 2019).

Fig. 6 shows both the total OLR anomalies from the seasonal cycle averaged from 0-25N, and the anomalies on the 10-20 day time scale (note the difference in color-scale) during the 2018 west Pacific monsoon season and PISTON period. Superimposed on these anomalies are the longitudinal positions of TC storm centers that entered the 0-25N latitude band during the period (Knapp et al. 2018, 2010). It can be seen that the TCs do occasionally project onto this timescale, but the 10-20 day band does include more than just propagating TCs (Ko and Hsu 2006, 2009). 10-20 day filtered anomalies during this period are generally westward-propagating, and consistently active throughout the monsoon season. This holds true when other years are selected, but only 2018 is shown here. Thus, the 2018 field campaign observed notable 10-20 variability in lower tropospheric winds (Fig. 5), which corresponds to westward propagating signals in OLR when filtered to this band (Fig. 6).

The evolution of our QBWO index through the field campaign is shown in Figure 7. It can be seen that prominent 10-20 day variability consistently projected onto the index during the two month period. QBWO activity generally moved through each of the phases in order, and remained in a single phase for 1-2 days. According to this index, the strongest period of activity that progressed through a complete cycle occurred from roughly 11 September to 23 September, with days at least one day in each phase and an amplitude ($a = \sqrt{PC1^2 + PC2^2}$) greater than 1.0 throughout the period.

CMORPH precipitation estimates averaged across latitude in Box M (Fig. 1) over Mindanao are shown for this highlighted 13-day period in Figure 8. Fig. 8b shows total column water vapor and 850-hPa zonal wind anomalies from the JJAS composite mean diurnal cycle from ERA5 averaged inside box M. Mindanao is shown here rather than Luzon because Typhoon Mangkhut made a direct landfall on 14 September. From 11 Sep to 15 Sep, Mindanao experienced strong westerly winds at 850-hPa with increased moisture. Concurrently, there was relatively little precipitation over the main island, with some heavy precipitation occurring over the Moro Gulf (Box D in Fig. 1) to the west. As the QBWO index moved through phases 7-8 on 15-16 September, drier conditions moved over Mindanao, and there was relatively little precipitation anywhere in the domain. Then from 17-20 September, the main island exhibited pronounced diurnal precipitation over the high topography, with westward propagation into the evening and overnight each day (most prominent on 17 Sep). Moisture was slightly higher than normal during this period, while winds started with easterly anomalies and transitioned to westerly anomalies by the 20th.

The end of the cycle from 21-23 September, during phases 4-5 in our index, displayed markedly different diurnal precipitation behavior. With weakly positive moisture anomalies and westerly wind anomalies, the diurnal cycle was relatively inactive over the Moro Gulf and western Mindanao (although there was some nocturnal precipitation on 22 Sep in the Moro Gulf), while the eastern coastline experienced strong evening precipitation each day, with some indication of propagation to the east into the Philippine Sea. Even from a short case study, these results are consistent with other studies pointing to high moisture and offshore lower tropospheric wind as environmental background conditions favoring a strong diurnal cycle, which here is related to 10-20 day variability (Vincent and Lane 2017; Natoli and Maloney 2019; Sakaeda et al. 2020).

The PISTON period is used in this study to show that 10-20 variability and its impact on the diurnal cycle can show up in raw data during a major field campaign and test our index during a real event. However, a two month period is not sufficient to draw robust conclusions. Thus, we will discuss a composite analysis based on the index described above in the following sections.

b. Large Scale

Variables are composited by each of the 8 phases of this index, with days on which the index amplitude is less than 1 excluded. The total number of days included in each composite can be found in Fig. 4. Figure 9 shows the large scale structure of the QBWO as captured by this index, with every other phase shown. Daily unfiltered OLR anomalies with ERA5 850-hPa vector wind anomalies superimposed are shown on the left, with ERA5 total column water vapor anomalies and total wind (not anomalies) on the right. The index captures the northwestward propagation of alternating zones of suppressed and enhanced convection, associated with anti-cyclonic and cyclonic wind anomalies respectively, consistent with QBWO structure observed in prior studies (Chen and Sui 2010; Qian et al. 2019; Yan et al. 2019).

Suppressed convection dominates much of the tropical western Pacific in phase 1, with anomalous easterly winds and dry air pushing across the region. The remnant of a westerly monsoon surge can be seen with southwesterly winds and moist conditions over the northern South China Sea and Taiwan. By phase 3, the suppressed convection and easterly anomalies are maximized over the northern Philippines, along with a significant dry anomaly. In total wind, this phase is characterized by trade easterlies dominating the entire domain outside of the mid-latitude westerlies on the northern fringes. Some indications of weakly enhanced convection begins to emerge in this phase around 10N, 145E. In phase 5, the enhanced convection becomes much more prominent, with a well defined anomalously cyclonic circulation centered over the Philippine Sea. Monsoon westerly winds start to strengthen over the Philippines and nearby waters, collocated with increasing moisture content. Enhanced convection, total column water, and westerly winds are maximized over the northern Philippines in phase 7, with an obvious monsoon surge penetrating deep into the Pacific. Overall, these structures are very similar to QBWO structures depicted in prior work (Chen and Sui 2010; Qian et al. 2019).

Figures 10 and 11 show the impact of the QBWO on precipitation across the Philippine archipelago. Daily mean precipitation anomalies generally follow the anomalies in column moisture shown in Fig. 9, consistent with many other studies highlighting the importance of moisture, particularly in the lower to middle free troposphere, for maintaining convection and precipitation (Bretherton et al. 2004; Holloway and Neelin 2009, 2010; Kuo et al. 2017; Vincent and Lane 2017). Enhanced precipitation is manifest in a southwest to northeast band that moves to the northwest. The vast majority of these points are statistically significant at the 95% confidence level determined via a bootstrapping method. An interesting exception is Mindanao in the southern Philippines (see Fig. 1), which generally does not follow the precipitation pattern of neighboring seas. There is some evidence that surges of the monsoon do not provide as significant a modulation of oceanic convection near and south of this island when compared to islands further north (Natoli and Maloney 2019; Xu et al. 2021).

The variability of the amplitude of the diurnal cycle through the QBWO cycle is noted in Fig. 11. Diurnal amplitude is defined in this study as the amplitude of the first diurnal harmonic of the composite diurnal cycle. A strong diurnal cycle begins to emerge over Mindanao in phase 2, peaking there in phase 3. This signal is also present in the Moro Gulf, the small body of water to the southwest of Mindanao, likely indicating offshore propagation from land-based convection (Natoli and Maloney 2019). The central Philippines and Luzon see strong diurnal cycles maximizing in Phases 4 and 5, still about 1/4 cycle ahead of the moisture maximum which occurs around phase

7. As in many prior studies examining the impact of the BSISO on the diurnal cycle in the 8-phase framework, the amplitude of the diurnal cycle over the northern Philippines (Figure 11) is not in phase with the daily mean precipitation (Peatman et al. 2014; Xu and Rutledge 2018; Natoli and Maloney 2019; Chudler et al. 2020). Despite widespread oceanic convection and abundant moisture in phase 7, the amplitude of the diurnal cycle is strongly suppressed over large islands of the Philippines. The strongest diurnal cycle tends to occur several phases before the maximum in daily mean precipitation and column moisture, when winds are still weakly easterly (Fig. 9f,g). Generally, this is consistent with the impact of the BSISO on the diurnal cycle. In subsequent sections, the differences between the diurnal cycle behavior associated with the QBWO and the BSISO are examined in detail with the goal of elucidating the mechanisms important to diurnal cycle regulation.

c. Luzon

Luzon is the largest and most populous island of the Philippines, and presents an excellent case for examining the diurnal cycle due to the north to south orientation of its coastline and mountain ranges (Fig. 1). Fig. 12 shows Hovmöller plots of composite diurnal cycles from each QBWO phase to better interpret offshore propagation. CMORPH precipitation rate is averaged across latitude inside box L (Fig. 1), which covers northern Luzon, and shows a strong diurnal cycle over land peaking in the late afternoon for all phases. While the diurnal cycle is present in all, there is variability in its prominence and behavior. Phase 3, for example, has a weaker precipitation maximum and some initial propagation offshore both east and west, but precipitation dissipates rather quickly. In phases 4 and 5 (which have the strongest diurnal cycle amplitude anomalies in Fig. 11), precipitation rate maximizes over the highest topography and then persists much later into the night while propagating offshore, with the westward direction favored. Oceanic precipitation increases further in phase 6, while phases 7-8 shows a constantly elevated precipitation rate offshore (particularly west of Luzon), with lesser diurnal variation. There still some evidence of a diurnal cycle over the highest elevations of the island.

While the diurnal cycle over western Luzon and the South China Sea appears to peak around phase 5, there is a notable asymmetry. The diurnal cycle on the eastern part of the island appears stronger in phase 1, with some weak propagation into the Philippine Sea. This asymmetry has also been noted for the impact of both the BSISO/MJO and some convectively coupled equatorial waves on the diurnal cycle (Ichikawa and Yasunari 2006, 2008; Sakaeda et al. 2017, 2020; Natoli and Maloney 2019), and warrants a closer look.

Figure 13 shows the diurnal cycle over certain subsets of the island, with boxes of spatial averaging shown in Fig. 1. Fig. 13a-c show the composite diurnal cycles in these boxes for select phases of the QBWO and the BSISO, according to the Lee et al. (2013) index. The orange lines show the phase with the largest diurnal range (difference between daily maximum and daily minimum precipitation rate) in the composite, while the blue lines show the phase with the smallest. These results were also considered for the diurnal amplitude, and the conclusions are similar. The right column shows the progression of the diurnal range and daily mean precipitation rate through each of the 8 phases of both indices.

The daily mean precipitation rates track together very closely between the BSISO and QBWO in Fig. 13d-f for each region. This indicates that the phase numbers are approximately equivalent in terms of proximity to the peak of the large scale convection associated with the feature of interest. Generally, daily mean precipitation varies slightly more strongly with QBWO phase than with BSISO, but the differences are modest. The diurnal range is also remarkably similar. Over northwest Luzon (Fig. 13e) and the coastal South China Sea (Fig. 13d), the largest range of the diurnal cycle leads the daily mean precipitation by about 1/4 cycle in both the QBWO index and the BSISO index. The magnitude of the change in diurnal range appears similar for both indices despite the slightly stronger modulation of the daily mean precipitation by the QBWO.

The details of the diurnal cycle (Fig. 13a-c) look remarkably similar as well. Over land in northwest Luzon (Fig. 13b), the highest amplitude phases have a sharply enhanced afternoon peak compared to the JJAS mean, but precipitation is strongly suppressed at all other times of the day. In the smallest diurnal range phases for each index, northwest Luzon sees consistently elevated precipitation rates throughout the day, with a slight bump during the evening peak that doesn't quite reach the JJAS mean precipitation rate at that time. The behavior over the South China Sea (Fig. 13b) is also similar, with phase 5 in each index exhibiting heavier precipitation during the typical peak of around 2100 when westward propagating precipitation arrives. Phase 1 in each index has a fairly constant precipitation rate all day, indicating that little convection that initiates over land is propagating offshore (as also seen in Fig. 12a).

The two modes also exhibit the same east/west asymmetry, with the largest diurnal ranges coming after the convective maximum for each index in the eastern part of the island. Over land in northeast Luzon (Fig. 13f), the strongest diurnal cycle occurs after the peak in daily mean precipitation, in phases 8 and 1 for the BSISO, and phases 1 and 2 for the QBWO. Precipitation rate over this region throughout the day (Fig. 13c) exhibits similar behavior at the end of the convective maximum (phases 8, 1, 2) compared with northwest Luzon (Fig. 13b) in the phases leading up to the convective maximum (phases 3-5) in both indices. This is consistent with conclusions drawn by Sakaeda et al. (2020) on diurnal cycle asymmetry through the passage of a large scale disturbance like the MJO or an R1 wave. Overall, the diurnal cycle behavior over Luzon associated with the QBWO index strongly resembles the results previously seen for the BSISO. This motivates the hypothesis that the impact on the diurnal cycle is not unique to either mode, rather, that each mode impacts the background state near Luzon similarly, leading to congruent diurnal cycle behavior.

d. Mindanao

In Mindanao, the diurnal cycle contributes much more to variability in daily mean precipitation than it does over Luzon (Natoli and Maloney 2019). As such, the disconnect between the diurnal range and daily mean precipitation is not as distinct as for Luzon. Figure 14 demonstrates that the amplitude of the diurnal cycle is more closely aligned with daily mean precipitation over Mindanao, whereas the diurnal amplitude leads the daily mean by about 1/4 cycle over Luzon. Daily mean precipitation in Mindanao is not in phase with the large-scale convective maximum over surrounding waters, as it is over Luzon. This discrepancy likely results from the fact that there is very little precipitation overnight over Mindanao in any phase, as the island appears to not receive as much oceanic precipitation during surges of the monsoon (Natoli and Maloney 2019 and their Figures 7 and 9). Xu et al. (2021) and their Figure 1 also shows that the difference between daily mean precipitation in the active BSISO compared to suppressed BSISO is much greater over the waters west of Luzon than near Mindanao.

While explaining the difference in oceanic precipitation is beyond the scope of this paper, we offer some hypotheses that the greater modulation of total column water vapor (Fig. 9) near Luzon compared to Mindanao may be responsible for this since ambient moisture is a strong control on tropical precipitation (Bretherton et al. 2004; Holloway and Neelin 2009, 2010). It is further speculated that the location of Borneo upstream of Mindanao during the active southwesterly monsoon flow may inhibit the moisture flux. This idea is consistent with recent work by Tan et al. (2021), who showed a systematic increase in precipitation downwind of an MC island when it was removed in a WRF simulation. Future experiments could follow the methods of Tan et al. (2021) applied to the boreal summer monsoon. The behavior of the diurnal cycle for both Luzon and Mindanao is quite similar, but the diurnal cycle appears to determine daily mean precipitation much more strongly over Mindanao considering its relative lack of nearby oceanic precipitation that could impact the island itself.

One interesting feature in Fig. 14 is that the BSISO has a noticeably stronger impact than the QBWO on both the diurnal range and (likely as a consequence) the daily mean precipitation rate in Mindanao. However, beyond the magnitude disparity, the diurnal cycle amplitude varies as a function of each index similarly here as in Luzon. It should be emphasized that due to its location further south, both the active QBWO and BSISO impact Mindanao in an earlier phase than Luzon, thus the phase numbers of an active event do not exactly align between the two islands. Over the central portion of the island (Box E in Fig. 1), a strong diurnal cycle is prominent in phase 3 for both modes of intraseasonal variability (ISV) (Fig. 14b,e), which is about 1/4 cycle before the large scale convective maximum in QBWO phase 5 (Fig. 6c). Fig. 14a,d shows that the timing of the strongest diurnal cycle in the Moro Gulf (Box D in Fig. 1) with respect to phase of the ISV mode follows that over land on the western shore, indicating likely offshore propagation.

The maximum diurnal cycle over eastern Mindanao Fig. 14c,f occurs in phases 4-5 for the QBWO and phase 8 for the BSISO, while the minimum occurs in phase 2 for both. BSISO phases 4 and 5 do experience a slight bump in the range of the diurnal cycle, but it it smaller than the QBWO increase in these phases, and smaller than the range in BSISO phase 8. In summary, the diurnal cycle behavior in Mindanao and Luzon progresses qualitatively similarly through a life cycle of both the QBWO and BSISO, with an elevated diurnal range occurring about 1/4 cycle before the large-scale convective maximum on the western side of the archipelago and over neighboring seas.

4. Discussion

a. Overview

In this section, we will compare and contrast the environmental background conditions associated with the QBWO and the BSISO in an effort to understand the mechanisms through which these large scale features regulate the diurnal cycle. We aim to support a hypothesis that the type of ISV mode itself is of secondary importance, and its impact on the background state through initiation of a monsoon surge is what helps determine the strength of the diurnal cycle. In other words, if two large-scale modes impact the local environmental background conditions in the same way, similar diurnal cycle behavior should be expected.

Figure 15 shows three environmental variables from ERA5 averaged in box L (northern Luzon, Fig. 1) for the left column, and in box M (Mindanao) for the right column. These variables were cited by (Natoli and Maloney 2019) to explain much of the variability in the diurnal cycle. Figure 16 shows maps for phases 3 and 7 (roughly corresponding to the convective minimum and maximum over Luzon shown in Fig. 9) to provide context. Results are composited by QBWO/BSISO phase, with the JJAS mean shown as the dotted black line. As defined by these indices, it is evident that the environmental conditions are modulated similarly by both modes, over both islands.

Environmental moisture, particularly in the lower to middle free troposphere, has been shown to be a primary control the strength and longevity on tropical convection (Bretherton et al. 2004; Holloway and Neelin 2009). A rich supply of moisture in the environment will promote heavy rainfall, and longer-lived convection that propagates further offshore overnight. Dry conditions may weaken convection through entrainment, resulting in weaker rain rates and thus a weaker diurnal cycle that dissipates more rapidly (Kuo et al. 2017). The second variable considered is surface downwelling shortwave radiation, which is primarily modulated by cloud cover. Some studies have identified higher insolation as being responsible for stronger diurnal cycles occurring in the suppressed phase of the MJO (Rauniyar and Walsh 2011; Peatman et al. 2014; Bergemann et al. 2015; Birch et al. 2016). During large-scale suppressed convection, the sky is relatively clear and the increased insolation promotes a stronger sea-breeze circulation, which then leads to an enhanced diurnal cycle. The last key variable is the lower tropospheric wind, considered in this study at 850-hPa. Onshore wind tends to inhibit the diurnal cycle on the windward side of an MC island, and enhance it on the leeward side, while also promoting leeward offshore propagation (Ichikawa and Yasunari 2006, 2008; Oh et al. 2012; Yanase et al. 2017; Sakaeda et al. 2020). A sufficiently strong background wind may ventilate the land surface and reduce the land-sea thermal contrast, leading to a weakened diurnal cycle (Shige et al. 2017; Wang and Sobel 2017; Qian 2020). Thus, sufficient ambient moisture, increased solar radiation, and weakly offshore winds each are proposed to promote a strong diurnal cycle over land (Vincent and Lane 2016). Propagation offshore to the west may be more sensitive to moisture content, given that afternoon convection develops over land (Hassim et al. 2016; Coppin and Bellon 2019).

b. QBWO and BSISO Similarities

Each mode strongly modulates total column water vapor (TCWV) over the Philippines (Figs. 15a,d, 16a-b,g-h). This is roughly in line with the large-scale convective maximum tracked by OLR (Figs. 9, 16c-d,i-j). Surface downwelling solar radiation is anti-correlated with TCWV, maximizing during the large-scale suppressed period, and minimizing on the cloudy days of the active state (Fig. 15b,e). The strongest diurnal cycles appear to occur when none of the above variables are strongly unfavorable, which materializes during the transition from suppressed to active large-scale convection for both modes. TCWV and insolation have competing influences, with the active phases of each mode exhibiting high TCWV, which supports diurnal precipitation

(Vincent and Lane 2016), and low insolation, which inhibits the diurnal cycle (Rauniyar and Walsh 2011; Peatman et al. 2014; Birch et al. 2016). Lower tropospheric wind perpendicular to the coast (zonal wind in this case, since the coastline is oriented north to south), can be invoked to explain why the transition from inactive to active is associated with stronger diurnal cycles than the opposite transition (Figs. 15c,f, 16e-f,k-l)

Both the QBWO and BSISO strongly modulate low-level wind over the Philippines. Over Luzon, both indices capture easterly wind anomalies at 850-hPa in phases 3-5, and westerly wind anomalies in phases 7, 8, and 1. The phases (4 and 5 in each index) with the strongest diurnal cycles over northwest Luzon are associated with easterly wind anomalies, and weak total easterly offshore winds. In the opposite transition (phase 1 of each index), Luzon experiences near average moisture and near average shortwave radiation, but the diurnal cycle amplitude is much weaker than phase 5 on the western coast and the SCS, associated with continued westerly wind anomalies (Figs. 11a,e, 12a,e, and 13d,e,). Thus, high amplitude diurnal cycles appear to occur on the leeward side of the island when neither moisture or insolation are strongly unfavorable, consistent with other studies exploring the MJO-diurnal cycle relationship (Virts et al. 2013; Qian 2020).

Offshore propagation is also similarly influenced by each mode. The phase numbers refer to the corresponding conditions for Luzon for both modes, but the mechanism is still valid for Mindanao approximately 2 phases earlier. When large-scale convection is strongly suppressed and winds are slightly anomalously easterly (phases 2-3, Fig. 9), precipitation still forms over land during the afternoon, but it dissipates quickly rather than propagating offshore (Figs. 12b,c, 13e). This section of the cycle is likely too dry for the most robust offshore propagation. The transition from suppressed to active (phases 4-5) exhibits continued strong diurnal cycles over land associated with easterly low-level wind anomalies, neutral insolation anomalies, and increasing moisture content. Offshore propagation to the west is most robust here (Figs. 12, 13d), as more moist air is entrained into developing convection (Hassim et al. 2016; Coppin and Bellon 2019). During the large-scale convective maximum (phases 6-7), moisture is plentiful, but strong onshore westerly winds and cloudy conditions inhibit the diurnal cycle despite abundant oceanic precipitation in the SCS. The opposite transition in both modes (phases 8, 1) experiences continuing westerly winds despite insolation becoming more favorable. The onshore wind reduces the diurnal cycle on the west (windward) side, but strong diurnal cycles can still be found on the east (leeward) side with weak leeward propagation into the Philippine Sea (Ichikawa and Yasunari 2006; Virts et al. 2013).

c. QBWO and BSISO Differences

There are also some subtle differences in diurnal cycle behavior for the QBWO versus the BSISO life cycles, possibly due to subtle differences in modulation of the environmental background conditions. The diurnal cycle amplitude over Mindanao in phases 3 and 4 of the QBWO is smaller than phases 3 and 4 of the BSISO (Fig. 14a-b,d-e) despite rather similar values of environmental moisture and isolation in each (Fig. 15d-e). However, the 850-hPa zonal wind appears to be more precisely in phase with the increase in moisture and cloudiness during a QBWO life cycle, with all three maximizing in phase 5 and minimizing in phase 1. For the BSISO, the increase in low level wind appears to lag the increase in moisture and cloudiness by one phase, resulting in more a more westerly wind in phases 3-5. Mindanao thus experiences more anomalously westerly winds during QBWO phases 3-5, corresponding to a weaker diurnal cycle compared to BSISO phases 3-5, and less anomalously westerly winds during QBWO phases 6-8, corresponding to a stronger (i.e. less suppressed) diurnal cycle compared to BSISO phases 6-8.

Moreover, despite the stronger modulation of moisture and insolation, the QBWO appears to modulate lower tropospheric zonal wind more weakly (Fig. 16e-f,k-j) over both islands. Such behavior could hint at a possible stronger diurnal cycle regulation by the low-level wind compared to the other variables, as the diurnal cycle amplitude varies similarly or even slightly less with QBWO phase compared to BSISO phase. It is also worth noting here that the spectral power of 850-hPa wind over Mindanao in the 10-15 day band cannot be statistically distinguished from red noise at the 90% confidence level (Fig. 2b). This is consistent with Mindanao observing noticeably greater maximum diurnal amplitude in the BSISO composites compared to the QBWO composites. The subtle difference in the timing and strength of the wind variability with the QBWO life cycle could present a plausible explanation for some of the differences in precipitation behavior. However, more work, particularly model sensitivity tests, would be required to address this more directly.

5. Conclusions

This study has examined the variability of the Philippine diurnal cycle on the quasi-biweekly (10-20 day) time scale. To the knowledge of the authors at the time of writing, this is the first study to explore the relationship between the quasi-biweekly oscillation (QBWO), a northwestward propagating mode of variability in tropical convection and wind in the northwest tropical Pacific, and the diurnal cycle of precipitation in this region. While the MJO/BSISO-diurnal cycle relationship has received considerable attention, comparatively little has been dedicated to the quasi-biweekly mode despite accounting for a similar or even larger slice of the variance in convection (Kikuchi and Wang 2009; Qian et al. 2019). These findings complement and are generally consistent with that of Sakaeda et al. (2020) who examined the variability in the diurnal cycle associated with several other large-scale modes of tropical variability. This study also extends some of their ideas to the Asian and west Pacific summer monsoon region. The main findings are summarized as follows:

- The Philippines and surrounding waters experience noteworthy variability in convection and wind on the 10-20 day timescale (Figs. 2, 6, and 8), and this was observed in the field during the 2018 campaign Propagation of Intraseasonal Tropical Oscillations (PISTON; Figs. 5 and 6; Sobel et al. 2021).

- A QBWO index is described that captures a northwestward propagating area of enhanced convection on 10-20 day timescales, associated with increased moisture, cyclonic vorticity, and a surge of southwesterly monsoon winds (Fig. 9).

- Daily mean precipitation over the Philippines and coastal waters tracks with the large-scale convective envelope, except over Mindanao (Fig. 10). This is similar to results seen for the BSISO (Natoli and Maloney 2019; Chudler et al. 2020; Xu et al. 2021), but the QBWO appears to have a slightly stronger impact over Luzon.

- The amplitude of the diurnal cycle on the west side of the Philippines is maximized during the late-suppressed stage and transition from suppressed to active convection (Figs. 11, 13, and 14).

- Prominent offshore propagation to the west into the South China Sea occurs when moisture and insolation are sufficiently high, and the low-level wind points offshore, which occurs during the transition to active convection (Figs. 12, 13a,d, 14a,d, 15). This is also consistent with findings for the BSISO, but the diurnal modulation by the QBWO appears to be slightly weaker over Mindanao (Fig. 14).

- The increase in moisture, cloudiness, and westerly winds arrive more or less in phase for the QBWO, while moisture leads by one phase for the BSISO (Fig. 15). This, combined with the slightly weaker modulation of low-level wind by the QBWO (Fig. 16) is hypothesized to explain why the QBWO does not modulate the amplitude of the diurnal cycle more strongly than the BSISO, particularly in Mindanao (Fig. 14).

These results show that the widely studied impact of the MJO/BSISO on the tropical diurnal cycle (e.g. Peatman et al. 2014; Vincent and Lane 2016, 2017; Sakaeda et al. 2017; Lu et al. 2019) is not unique to this phenomenon, complementing several other studies exploring distinct modes of variability and their impacts on local scale precipitation (Ferrett et al. 2019; Sakaeda et al. 2020). We hypothesize that the large scale mode is rather unimportant beyond its impact on the environmental background conditions to the island of interest, namely, low-level wind, free tropospheric moisture, and insolation.

Heavy daily mean precipitation (Fig. 10), unsurprisingly, appears to closely follow total column water vapor (Fig. 9; Bretherton et al. 2004; Holloway and Neelin 2009, 2010; Kuo et al. 2017), with some orographic adjustments based on prevailing wind. The amplitude of the diurnal cycle and its longevity when propagating offshore appear to be strongly related to competing the influences of insolation and moisture (which support the diurnal cycle but are out of phase with one another), and onshore wind (which inhibits the diurnal cycle and offshore propagation by decreasing the land-sea thermal contrast and thus the sea-breeze; e.g. Wang and Sobel 2017; Qian 2020). The strongest diurnal cycles with most pronounced offshore propagation generally occur on days with average to above average moisture, sufficient insolation, and weakly offshore prevailing wind. This is found for both the QBWO and the BSISO.

Testing the relative contributions of each of these key variables identified here is the subject of ongoing analysis. While we have hypothesized a possible connection between these key variables and the diurnal cycle behavior based on observations of very similar modulation by both the QBWO and the BSISO, this analysis is insufficient to make more definitive statements and determine causality. Consequently, we anticipate that our ongoing work isolating the response of the diurnal cycle to these variables in high resolution models will provide additional insight.

Acknowledgments. This work was supported by the Office of Naval Research (ONR) under the Propagation of Tropical Intraseasonal Oscillations (PISTON) project N00014-16-1-3087, the NOAA CVP program under grant NA18OAR4310299, NASA CYGNSS grant 80NSSC21K1004, and the Climate and Large Scale Dynamics Program of the National Science Foundation under grant AGS-1735978. The authors would like to thank Paul Ciesielski for his work on processing and quality control of the PISTON sounding data.

Data availability statement. Sounding data from the PISTON field campaign can be found at https://www-air.larc.nasa.gov/cgi-bin/ArcView/camp2ex. CMORPH bias-corrected precipitation data as described in Xie et al. (2017) can be downloaded at https://www.ncei.noaa.gov/data/cmorph-high-resolution-global-precipitation-estimates/access/30min/8km/. ERA5 data as described in Hersbach et al. (2020) can be download at https://www.ecmwf.int/en/forecasts/datasets/reanalysis-datasets/era5. OLR data as described in Liebmann and Smith (1996) can be downloaded at https://psl.noaa.gov/data/gridded/data.interp_OLR.html. IBTrACS data as described in Knapp et al. (2010) can be found at https://www.ncdc.noaa.gov/ibtracs/.

References

Adler, R. F., and Coauthors, 2003: The version-2 global precipitation climatology project (GPCP) monthly precipitation analysis (1979-present). *J. Hydrometeor.*, **4**, 1147–1167.

Annamalai, H., and J. M. Slingo, 2001: Active / break cycles: diagnosis of the intraseasonal variability of the Asian Summer Monsoon. *Climate Dyn.*, **18**, 85–102.

Bagtasa, G., 2017: Contribution of tropical cyclones to rainfall in the Philippines. *J. Climate*, **30**, 3621–3633.

Bagtasa, G., 2019: Enhancement of summer monsoon rainfall by tropical cyclones in northwestern Philippines. *J. Meteor. Soc. Japan*, **97**, 967–976.

Bagtasa, G., 2020: Influence of Madden-Julian Oscillation on the intraseasonal variability of summer and winter monsoon rainfall in the Phillippines. *J. Climate*, **33**, 9581–9594.

Bergemann, M., C. Jakob, and T. P. Lane, 2015: Global detection and analysis of coastline-associated rainfall using an objective pattern recognition technique. *J. Climate*, **28**, 7225–7236.

Birch, C. E., S. Webster, S. C. Peatman, D. J. Parker, A. J. Matthews, Y. Li, and M. E. E. Hassim, 2016: Scale interactions between the MJO and the western Maritime Continent. *J. Climate*, **29**, 2471–2492.

Bretherton, C. S., M. E. Peters, and L. E. Back, 2004: Relationships between water vapor path and precipitation over the tropical oceans. *J. Climate*, **17**, 1517–1528.

Cayanan, E. O., T.-C. Chen, J. C. Argete, M.-C. Yen, and P. D. Nilo, 2011: The effect of tropical cyclones on southwest monsoon rainfall in the Philippines. *J. Meteor. Soc. Japan*, **89A**, 123–139.

Chatterjee, P., and B. N. Goswami, 2004: Structure, genesis and scale selection of the tropical quasi-biweekly mode. *Quart. J. Roy. Meteor. Soc.*, **130**, 1171–1194.

Chen, G., and C.-H. Sui, 2010: Characteristics and origin of quasi-biweekly oscillation over the western North Pacific during boreal summer. *J. Geophys. Res.*, **115**, D14 113.

Chen, R., Z. Wen, and R. Lu, 2016: Evolution of the circulation anomalies and the quasi-biweekly oscillations associated with extreme heat events in southern China. *J. Climate*, **29**, 6909–6921.

Chen, T.-C., and J.-M. Chen, 1993: The 10-20 day mode of the 1979 Indian Monsoon: Its relation with the time variation of monsoon rainfall. *Mon. Wea. Rev.*, **121**, 2465–2482.

Chen, T.-C., and J.-M. Chen, 1995: An observational study of the South China Sea monsoon during the 1979 summer: Onset and life cycle. *Mon. Wea. Rev.*, **123**, 2295–2318.

Chen, T.-C., M.-C. Yen, and S.-P. Weng, 2000: Interaction between the summer monsoons in east Asia and the South China Sea: Intraseasonal monsoon modes. *J. Atmos. Sci.*, **57**, 1373–1392.

Chudler, K., and S. A. Rutledge, 2021: The coupling between convective variability and large-scale flow patterns observed during PISTON 2018-2019. *J. Climate*, in press.

Chudler, K., W. Xu, and S. A. Rutledge, 2020: Impact of the Boreal Summer Intraseasonal Oscillation on the diurnal cycle of precipitation near and over the island of Luzon. *Mon. Wea. Rev.*, **148**, 1805–1827.

Ciesielski, P. E., and Coauthors, 2014: Quality-controlled upper-air sounding dataset for DYNAMO/CINTY/AMIE: development and corrections. *J. Atmos. Oceanic Technol.*, **31**, 741–764.

Copernicus Climate Change Service (C3S), 2017: ERA5: Fifth generation of ECMWF atmospheric reanalyses of the global climate. Copernicus Climate Change Service Climate Data Store (CDS), URL https://cds.climate.copernicus.eu/cdsapp#!/home, accessed 16 February 2021.

Coppin, D., and G. Bellon, 2019: Physical Mechanisms Controlling the Offshore Propagation of Convection in the Tropics: 1. Flat Island. *J. Adv. Model. Earth Syst.*, **11**, 3042–3056.

Cruz, F. T., G. T. Narisma, M. Q. V. II, K. U. C. Chua, and L. M. Olaguera, 2013: A climatological analysis of the southwest monsoon rainfall in the Philippines. *Atmos. Res.*, **122**, 609–616.

Duchon, C. E., 1979: Lanczos filtering in one and two dimensions. *J. Appl. Meteor.*, **18**, 1016–1022.

Ferrett, S., G.-Y. Yang, S. J. Woolnough, J. Methven, K. Hodges, and C. E. Holloway, 2019: Linking extreme preciptiation in Southeast Asia to equatorial waves. *Quart. J. Roy. Meteor. Soc.*, **146**, 665–684.

Fujita, M. K., K. Yoneyama, S. Mori, T. Nasuno, and M. Satoh, 2011: Diurnal convection peaks over the eastern Indian Ocean off Sumatra during different MJO phases. *J. Meteor. Soc. Japan*, **89A**, 317–330.

Gao, M., J. Yang, B. Wang, S. Zhou, D. gong, and S.-J. Kim, 2018: How are heat waves over Yangtze River valley associated with atmospheric quasi-biweekly oscillation? *Clim. Dyn.*, **51**, 4421–4437.

Gill, A. E., 1980: Some simple solutions for heat-induced tropical circulation. *Quart. J. Roy. Meteor. Soc.*, **106**, 447–462.

Gilman, D. L., F. J. Fuglister, and J. M. M. Jr., 1963: On the power spectrum of "Red Noise". *J. Atmos. Sci.*, **20**, 182–184.

Han, X., H.Zhao, X. Li, G. B. Raga, C. Wang, and Q. Li, 2020: Modulation of boreal extended summer tropical cyclogenesis over the northwest Pacific by the quasi-biweekly oscillation under different El Niño-southern oscillation phases. *Int. J. Climatol.*, **40**, 858–873.

Hassim, M. E. E., T. P. Lane, and W. W. Grabowski, 2016: The diurnal cycle of rainfall over New Guinea in convection-peritting WRF simulations. *Atmos. Chem. Phys.*, **16**, 161–175.

Hersbach, H., and Coauthors, 2020: The ERA5 global reanalysis. *Quart. J. Roy. Meteor. Soc.*, **146**, 1999–2049.

Ho, C.-H., M.-S. Park, Y.-S. Choi, and Y. N. Takayabu, 2008: Relationship between intraseasonal oscillation and diurnal variation of summer rainfall over the South China Sea. *Geophys. Res. Lett.*, **35**, L03 701.

Holloway, C. E., and J. D. Neelin, 2009: Moisture vertical structure, column water vapor, and tropical deep convection. *J. Atmos. Sci.*, **66**, 1665–1683.

Holloway, C. E., and J. D. Neelin, 2010: Temporal relations of column water vapor and tropical precipitation. *J. Atmos. Sci.*, **67**, 1091–1105.

Houze, R. A., S. G. Geotis, F. D. M. Jr., and A. K. West, 1981: Winter monsoon convection in the vicinity of north Borneo. Part I: Structure and time variation of the clouds and precipitation. *Mon. Wea. Rev.*, **109**, 1595–1614.

Huffman, G. J., and Coauthors, 2015: NASA Global Precipitation Measurement (GPM) Integrated Multi-satellitE Retrievals for GPM (IMERG). Algorithm Theoretical Basis Doc. (ATBD), version 06, 39 pp., accessed 7 July 2021.

Ichikawa, H., and T. Yasunari, 2006: Time-space characteristics of diurnal rainfall over Borneo and surrounding oceans as observed by TRMM-PR. *J. Climate*, **19**, 1238–1260.

Ichikawa, H., and T. Yasunari, 2008: Intraseaonal variability in diurnal rainfall over New Guinea and the surrounding oceans during austral summer. *J. Climate*, **21**, 2852–2868.

Joyce, R. J., J. E. Janowiak, P. A. Arkin, and P. Xie, 2004: CMORPH: A method that produces global precipitation estimates from passive microwave and infrared data at high spatial and temporal resolution. *J. Hydrometeor.*, **5**, 487–503.

Kikuchi, K., and B. Wang, 2009: Global perspective of the quasi-biweekly oscillation. *J. Climate*, **22**, 1340–1359.

Knapp, K. R., H. J. Diamond, J. P. Kossin, M. C. Kruk, and C. J. Schreck, 2018: NCDC International Best Track Archive for Climate Stewardship (IBTrACS) Project, Version 4. NOAA National Centers for Environmental Information, accessed 8 July 2021.

Knapp, K. R., M. C. Kruk, D. H. Levinson, H. J. Diamond, and C. J. Neumann, 2010: The International Best Track Archive for Climate Stewardship (IBTrACS): Unifying tropical cyclone best track data. *Bull. Amer. Meteor. Soc.*, **91**, 363–376.

Ko, K.-C., and H.-H. Hsu, 2006: Sub-monthly circulation features associated with Tropical Cyclone tracks over the East Asian monsoon area during July-August season. *J. Meteor. Soc. Japan*, **84**, 871–889.

Ko, K.-C., and H.-H. Hsu, 2009: ISO modulation on the submonthly wave pattern and recurving tropical cyclones in the tropical western North Pacific. *J. Climate*, **22**, 582–599.

Krishnamurti, T. N., and P. Ardanuy, 1980: The 10 to 20-day westward propagating mode and "Breaks in the Monsoons". *Tellus*, **32**, 15–26.

Krishnamurti, T. N., and H. N. Bhalme, 1976: Oscillations of a monsoon system. part i. observational aspects. *J. Atmos. Sci.*, **33**, 1937–1954.

Krishnamurti, T. N., P. K. Jayakumar, J. Sheng, N. Surgi, and A. Kumar, 1985: Divergent circulations on the 30 to 50 day time scale. *J. Atmos. Sci.*, **42**, 364–375.

Kuo, Y.-H., J. D. Neelin, and C. R. Mechoso, 2017: Tropical convection transition statistics and causality in the water vapor-precipitation relation. *J. Atmos. Sci.*, **74**, 915–931.

Lau, K.-M., and P. H. Chan, 1986: Aspects of the 40-50 day oscillation during the northern summer as inferred from outgoing longwave radiation. *Mon. Wea. Rev.*, **114**, 1354–1367.

Lawrence, D. M., and P. J. Webster, 2002: The Boreal Summer Intraseasonal Oscillation: Relationship between northward and eastward movement of convection. *J. Atmos. Sci.*, **59**, 1593–1606.

Lee, J.-Y., B. Wang, M. C. Wheeler, X. Fu, D. E. Waliser, and I.-S. Kang, 2013: Real-time multivariate indices for the boreal summer intraseasonal oscillation over the Asian summer monsoon region. *Climate Dyn.*, **40**, 493–509.

Li, K., Y. Yang, L. Feng, W. Yu, and S. Liu, 2020: Structures and northward propagation of the Quasi-Biweekly oscillation in the western north Pacific. *J. Climate*, **33**, 6873–6888.

Liebmann, B., and C. A. Smith, 1996: Description of a complete (interpolated) outgoing longwave radiation dataset. *Bull. Amer. Meteor. Soc.*, **77**, 1275–1277.

Liu, H.-B., J. Yang, D.-L. Zhang, and B. Wang, 2014: Roles of synoptic to quasi-biweekly disturbances in generating the summer 2003 heavy rainfall in east China. *Mon. Wea. Rev.*, **142**, 886–904.

Love, B. S., A. J. Matthews, and G. M. S. Lister, 2011: The diurnal cycle of precipitation over the Maritime Continent in a high resolution f model. *Quart. J. Roy. Meteor. Soc.*, **137**, 934–947.

Lu, J., T. Li, and L. Wang, 2019: Precipitation diurnal cycle over the Maritime Continent modulated by the MJO. *Clim. Dyn.*, **53**, 6489–6501.

Madden, R. A., and P. R. Julian, 1971: Detection of a 40-50 day oscillation in the zonal wind in the tropical Pacific. *J. Atmos. Sci.*, **28**, 702–708.

Mapes, B. E., T. T. Warner, and M. Xu, 2003: Diurnal patterns of rainfall in northwestern South America. Part III: Diurnal gravity waves and nocturnal convection offshore. *Mon. Wea. Rev.*, **131**, 830–844.

Matsumoto, J., L. M. P. Olaguera, D. Nguyen-Le, H. Kubota, and M. Q. V. II, 2020: Climatological seasonal changes of wind and rainfall in the Philippines. *Int. J. Climatol.*, **40**, 4843–4857.

Matsuno, T., 1966: Quasi-geostrophic motions in the equatorial area. *J. Meteor. Soc. Japan*, **44**, 25–43.

Mori, S., J.-I. Hamada, Y. I. Tauhid, and M. D. Yamanaka, 2004: Diurnal land-sea rainfall peak migration over Sumatera island, Indonesian Maritime Continent, observed by TRMM satellite and intensive rawinsonde soundings. *Mon. Wea. Rev.*, **132**, 2021–2039.

Moron, V., A. Lucero, F. Hilario, B. Lyon, A. W. Robertson, and D. DeWitt, 2009: Spatio-temporal variability and predictability of summer monsoon onset over the Philippines. *Clim. Dyn.*, **33**, 1159–1177.

National Geophysical Data Center, 2006: 2-minute Gridded Global Relief Data (ETOPO2)v2. NOAA, accessed 12 February 2018, doi:10.7289/V5J1012Q.

Natoli, M. B., and E. D. Maloney, 2019: Intraseasonal variability of the diurnal cycle of precipitation in the Philippines. *J. Atmos. Sci.*, **76**, 3633–3654.

Oh, J.-H., K.-Y. Kim, and G.-H. Lim, 2012: Impact of MJO on the diurnal cycle of rainfall over the western Maritime Continent in the austral summer. *Climate Dyn.*, **38**, 1167–1180.

Ohsawa, T., H. Ueda, T. Hayashi, A. Watanabe, and J. Matsumoto, 2001: Diurnal variations of convective activity and rainfall in tropical Asia. *J. Meteor. Soc. Japan*, **79B**, 333–352.

Olaguera, L. M. P., J. Matsumoto, H. Kubota, E. O. Cayanan, and F. D. Hilario, 2020: A climatological analysis of the monsoon break following the summer monsoon onset over Luzon Island, Philippines. *Int. J. Climatol.*, **41**, 2100–2117.

Park, M.-S., C.-H. Ho, J. Kim, and R. L. Elsberry, 2011: Diurnal circulations and their multi-scale interaction leading to rainfall over the South China Sea upstream of the philippines during intraseasonal monsoon westerly wind bursts. *Climate Dyn.*, **37**, 1483–1499.

Peatman, S. C., A. J. Matthews, and D. P. Stevens, 2014: Propagation of the Madden-Julian Oscillation through the Maritime Continent and scale interaction with the diurnal cycle of precipitation. *Quart. J. Roy. Meteor. Soc.*, **140**, 814–825.

Qian, J., 2008: Why precipitation is mostly concentrated over islands in the Maritime Continent. *J. Atmos. Sci*, **65**, 1428–1441.

Qian, J. H., 2020: Mechanisms for the dipolar patterns of rainfall variability over large islands in the Maritime Continent associated with the Madden-Julian oscillation. *J. Atmos. Sci.*, **77**, 2257–2278.

Qian, Y., P.-C. Hsu, and K. Kikuchi, 2019: New real-time indices for the quasi-biweekly oscillation over the Asian summer monsoon region. *Clim. Dyn.*, **53**, 2603–2624.

Ramage, C. S., 1968: Role of a tropical "Maritime Continent" in the atmospheric circulation. *Mon. Wea. Rev.*, **96**, 365–370.

Rauniyar, S. P., and K. J. E. Walsh, 2011: Scale interaction of the diurnal cycle of rainfall over the Maritime Continent and Australia: Influence of the MJO. *J. Climate*, **24**, 325–348.

Riley Dellaripa, E. M., E. D. Maloney, B. A. Toms, S. M. Saleeby, and S. C. van den Heever, 2020: Topographic effects on the Luzon diurnal cycle during the BSISO. *J. Atmos. Sci.*, **77**, 3–30.

Sahlu, D., E. I. Nikolopoulos, S. A. Moges, E. N. Anagnostou, and D. Hailu, 2016: First evaluation of the day-1 IMERG over the upper Blue Nile basin. *J. Hydrometeor.*, **17**, 2875–2882.

Sakaeda, N., G. Kiladis, and J. Dias, 2020: The diurnal cycle of rainfall and the convectively coupled equatorial waves over the Maritime Continent. *J. Climate*, **33**, 3307–3331.

Sakaeda, N., G. N. Kiladis, and J. Dias, 2017: The diurnal cycle of tropical cloudiness and rainfall assocaited with the Madden-Julian oscillation. *J. Climate*, **30**, 3999–4020.

Sakurai, N., and Coauthors, 2005: Diurnal cycle of cloud system migration over sumatera island. *J. Meteor. Soc. Japan*, **83**, 835–850.

Shige, S., Y. Nakano, and M. K. Yamamoto, 2017: Role of orography, diurnal cycle, and intraseasonal oscillation in summer monsoon rainfall over the Western Ghats and Myanmar coast. *J. Climate*, **30**, 9365–9381.

Sobel, A. H., J. Sprintall, E. D. Maloney, Z. K. Martin, S. Wang, S. P. de Szoeke, B. C. Trabing, and S. A. Rutledge, 2021: Large-scale state and evolution of the atmosphere and ocean during PISTON 2018. *J. Climate*, **34**, 5017–5035.

Sui, C.-H., and K.-M. Lau, 1992: Multiscale phenomena in the tropical atmosphere over the western Pacific. *Mon. Wea. Rev.*, **120**, 407–430.

Tan, H., P. Ray, B. Barrett, J. Dudhia, and M. W. Moncrieff, 2021: Systematic patterns in land precipitation due to convection in neighboring islands in the Maritime Continent during MJO Propagation. *J. Geophys. Res. Atmos.*, **126**, e2020JD033 465.

Tao, L., X. Fu, and W. Lu, 2009: Moisture structure of the quasi-biweekly mode revealed by AIRS in western Pacific. *Adv. Atmos. Sci.*, **26**, 513–522.

Vincent, C. L., and T. P. Lane, 2016: Evolution of the diurnal precipitation cycle with the passage of a Madden-Julian oscillation event through the Maritime Continent. *Mon. Wea. Rev.*, **144**, 1983–2005.

Vincent, C. L., and T. P. Lane, 2017: A 10-Year Austral summer climatology of observed and modeled intraseasonal, mesoscale, and diurnal variations over the Maritime Continent. *J. Climate*, **30**, 3807–3828.

Virts, K. S., J. M. Wallace, M. L. Hutchins, and R. H. Holzworth, 2013: Diurnal lightning variability over the Maritime Continent: Impact of low-level winds, cloudiness, and the MJO. *J. Atmos. Sci.*, **70**, 3128–3146.

Wang, S., and A. H. Sobel, 2017: Factors controlling rain on small tropical islands: Diurnal cycle, large-scale wind speed, and topography. *J. Atmos. Sci.*, **74**, 3515–3532.

Wheeler, M., and H. H. Hendon, 2004: An all-season real-time multivariate MJO index: Development of an index for monitoring and prediction. *Mon. Wea. Rev.*, **132**, 1917–1932.

Wu, P., D. Ardiansyah, S. Yokoi, S. Mori, F. Syamsudin, and K. Yoneyama, 2017: Why torrential rain occurs on the western coast of Sumatra island at the leading edge of the MJO westerly wind bursts. *SOLA*, **13**, 36–40.

Wu, P., M. Hara, J.-I. Hamada, M. D. Yamanaka, and F. Kimura, 2009: Why a large amount of rain falls over the vicinity of western Sumatra island during nighttime. *J. Appl. Meteor. Climatol.*, **48**, 1345–1361.

Wu, P., S. Mori, and F. Syamsudin, 2018: Land-sea surface air temperature contrast on the western coast of Sumatra island during an active phase of the Madden-Julian Oscillation. *Prog. Earth Planet. Sci.*, **5**, 4.

Xie, P., R. Joyce, S. Wu, S.-H. Yoo, Y. Yarosh, F. Sun, and R. Lin, 2017: Reprocessed, bias-corrected CMORPH global high-resolution precipitation estimates from 1998. *J. Hydrometeor.*, **18**, 1617–1641.

Xu, W., and S. A. Rutledge, 2018: Convective variability associated wit the Boreal Summer Intraseasonal Oscillation in the South China Sea region. *J. Climate*, **31**, 7363–7383.

Xu, W., S. A. Rutledge, and K. Chudler, 2021: Diurnal cycle of coastal convection in the South China Sea Region and modulation by the BSISO. *J. Climate*, **34**, 4297–4314.

Yan, X., S. Yang, T. Wang, E. D. Maloney, S. Dong, W. Wei, and S. He, 2019: Quasi-biweekly oscillation of the Asian monsoon rainfall in late summer and autumn: different types of structure and propagation. *Clim. Dyn.*, **53**, 6611–6628.

Yanase, A., K. Yasunaga, and H. Masunaga, 2017: Relationship between the direction of diurnal rainfall migration and the ambient wind over the southern Sumatra island. *Earth and Space Science*, **4**, 117–127.

Yang, J., B. Wang, and B. Wang, 2008: Anticorrelated intensity change of the quasi-biweekly and 30-50-day oscillations over the South China Sea. *Geophys. Res. Lett.*, **35**, L16 702.

Yusef, A. A., and H. Francisco, 2009: Climate change vulnerability mapping for Southeast Asia, Economy and Environment Program for Southeast Asia (EEPSEA) report, June 2009. Economy and Environment Program for Southeast Asia, available online at http://www.eepsea.org, 32pp pp.

Zhou, H., P.-C. Hsu, and Y. Qian, 2018: Close linkage between quasi-biweekly oscillation and tropical cyclone intensification over the western north pacific. *Atmos. Sci. Lett.*, **19**, e826.

Zhu, L., Z. Meng, F. Zhang, and P. M. Markowski, 2017: The influence of sea- and land-breeze circulations on the diurnal variability in precipitation over a tropical island. *Atmos. Chem. Phys.*, **17**, 13 213–13 232.

LIST OF FIGURES

Fig. 1. NOAA ETOPO2 Topography (in meters) over the Philippines, with boxes of spatial averaging and important geographic features noted. The track of the R/V Thomas G. Thompson during the August-October 2018 PISTON field campaign is also shown in purple, with August in the darkest color and October in the lightest. 44

Fig. 2. (a) Power spectrum of ERA5 850-mb zonal wind averaged inside box L in Fig. 1 during June-September (JJAS) 1998-2020 (blue), with theoretical red noise spectrum (red; Gilman et al. 1963), and its 90% confidence bound calculated with an F-test (gray, dotted). (b) As in (a) but for Mindanao, averaged inside box M. 45

Fig. 3. Spatial pattern at -4 (top), -2 (middle), and 0-day (bottom) lags from extended EOFs 1 (left) and 2 (right) of 10-20 day bandpass filtered AVHRR OLR anomalies in physical units (W m^{-2}). The bottom row shows the difference between power spectra of each corresponding principal component time series and the corresponding 90% confidence bound of a theoretical red noise spectrum with the same autocorrelation as the PC time series. Values above zero (dotted red line) can be considered statistically significant at the 90% confidence level. . . . 46

Fig. 4. Number of days in a certain Lee et al. (2013) BSISO phase distributed by active QBWO phase. The BSISO is considered to be inactive when the amplitude of the index is less than one. The darker color in the stacked bar chart indicates days that are classified as the same phase number in both indices. 47

Fig. 5. Time-height diagram of zonal wind from each sounding taken as part of the PISTON field campaign between 14 August 2018 and 13 October 2018. Soundings were taken every 12 hours from the island of Yap (top) and every 3 hours from the R/V Thomas G. Thompson during operational periods (bottom). 48

Fig. 6. Hovmöller plot of AVHRR OLR averaged between 0 and 25N at each longitude during 1 June-20 October 2018, bandpass filtered to the 10-20 day timescale using a Lanczos filter with 93 weights in W m^{-2} (left), and OLR anomalies from the seasonal cycle defined by the average daily climatology smoothed with a 7-day running mean (right). Named tropical cyclone tracks from IBTrACS are superimposed with gray dotted lines when the storm center was inside 0-25N. 49

Fig. 7. Phase space diagram of the QBWO index activity from 14 August-14 October 2018 (the PISTON field campaign period), with the first principal component on the y-axis and the second principal component on the x-axis. The split between the 8 phases is denoted with black dotted lines, while days with an amplitude less than 1 (inside the center circle) are considered inactive, and not part of any phase. August is shown in the darkest color, with October in the lightest pink. The corresponding numbers indicate the date of each month. . . 50

Fig. 8. (a) CMORPH precipitation rate estimates (mm/hr) averaged from 6N-8N across Mindanao (Box M, Fig. 1) from 11 September 2018 to 23 September 2018, during one full cycle of the QBWO index. The average topography in this box from NOAA ETOPO2 is shown on the bottom, with the coastlines drawn as vertical dashed black lines. Note that there are some land points west of the western coastline here, part of the Zamboanga Peninsula. The horizontal dashed black lines correspond to 00 UTC, or 0800 local time. (b) Zonal wind at 850-hPa averaged across both latitude and longitude in Box M (red line) and total column water vapor (blue line) from ERA5, with the JJAS composite diurnal cycle removed at each hour. 51

Fig. 9. Composite maps by select QBWO phase over the West Pacific ocean of anomalies of OLR (W m^{-2}) and vector anomalies of 850-mb wind from ERA5 (left column), and anomalies of ERA5 total column water vapor (kg m^{-2}) with total 850-mb vector wind (right column). The total number of days in each composite can be ascertained from Figure 4 52

Fig. 10. Anomalies in daily mean CMORPH precipitation rate composited by QBWO phase, with statistical significance at the 95% confidence level shown as dots. 53

Fig. 11. Anomalies in the amplitude of the CMORPH precipitation rate diurnal cycle by QBWO phase. Anomalies are calculated as the difference in diurnal amplitude between each phase composite, and amplitude of the JJAS composite diurnal cycle. Statistical significance at the 95% confidence level is shown as dots. 54

Fig. 12. Hovmöller diagrams of the composite diurnal cycle of CMORPH precipitation rate (mm/day) for select phases of the QBWO index calculated by projecting unfiltered OLR anomalies onto the EEOF spatial patterns shown in Fig. 3 (top), and the index calculated by projecting 10-20 day bandpass filtered OLR anomalies onto the same EEOF patterns (bottom). Precipitation rates are averaged across latitude in box L (Fig. 1), with corresponding longitude noted below. The average elevation of topography from NOAA ETOPO2 inside box L is shown at the bottom for reference. 55

Fig. 13. (a-c) Composites of the spatially averaged diurnal cycle of CMORPH precipitation rate (mm/day) in the QBWO (solid) and Lee et al. (2013) BSISO (dotted) phase with the highest diurnal range (orange), the QBWO/BSISO phase with the smallest diurnal range (blue), and the full JJAS composite (dotted black). Spatial averaging is done over ocean points inside box A (a), and land points inside boxes B (b) and C (c). (d-f) The corresponding daily mean precipitation (blue) and diurnal range (red) in mm/day of each phase's spatially averaged composite diurnal cycle, by QBWO phase (solid) and BSISO phase (dotted). Each box covers a domain near Luzon. 56

Fig. 14. (a-c) Composites of the spatially averaged diurnal cycle of CMORPH precipitation rate (mm/day) in the QBWO (solid) and Lee et al. (2013) BSISO (dotted) phase with the highest diurnal range (orange), the QBWO/BSISO phase with the smallest diurnal range (blue), and the full JJAS composite (dotted black). Spatial averaging is done over ocean points inside box D (a), and land points inside boxes E (b) and F (c). (d-f) The corresponding daily mean precipitation (blue) and diurnal range (red) in mm/day of each phase's spatially averaged composite diurnal cycle, by QBWO phase (solid) and BSISO phase (dotted). As in Fig. 13 but for Mindanao. 57

Fig. 15. Daily mean values of select variables from ERA5 composited by QBWO phase (solid, orange) and BSISO phase (dotted, blue), averaged over box L covering Luzon (left) and box M covering Mindanao (right). Total column water vapor (kg m^{-2}) is shown on top (a, d), downwelling shortwave radiation (W m^{-2}) at the surface in the middle row (b, e), and 850-hPa zonal wind (m s^{-2}) at the bottom (c, f). Corresponding JJAS mean values for each variable on each island are shown as a horizontal dotted black line. 58

Fig. 16. Daily mean anomalies from JJAS average of select variables from ERA5 composited by QBWO phase (top) and BSISO phase (bottom) over the Philippines. For each variables, phase 3 of each index is shown at the left, and phase 7 at the right. The grouping of 4 panels at the left shows total column water vapor (kg m^{-2}), the middle grouping shows downwelling shortwave radiation (W m^{-2}) at the surface, and the right grouping shows 850-hPa zonal wind (m s^{-2}). 59

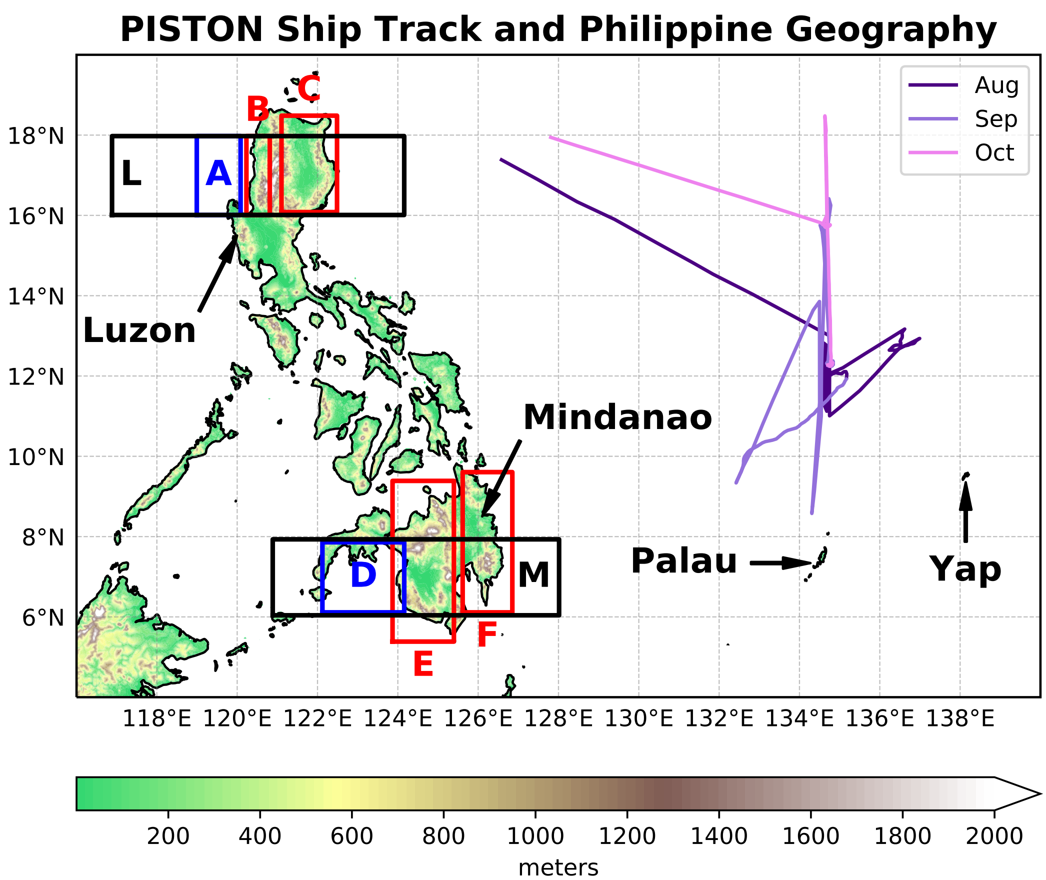

FIG. 1. NOAA ETOPO2 Topography (in meters) over the Philippines, with boxes of spatial averaging and important geographic features noted. The track of the R/V Thomas G. Thompson during the August-October 2018 PISTON field campaign is also shown in purple, with August in the darkest color and October in the lightest.

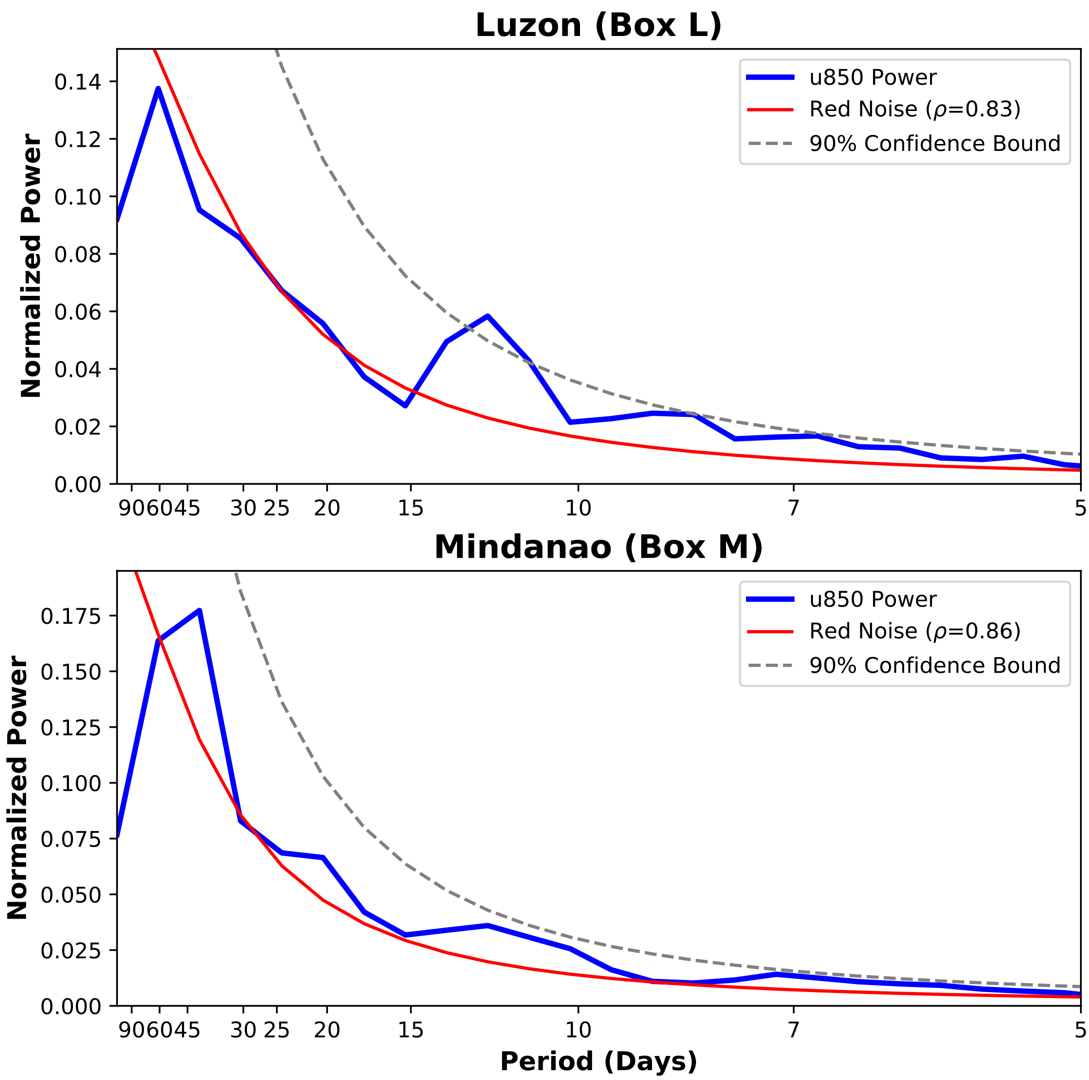

994 FIG. 2. (a) Power spectrum of ERA5 850-mb zonal wind averaged inside box L in Fig. 1 during June-September
995 (JJAS) 1998-2020 (blue), with theoretical red noise spectrum (red; Gilman et al. 1963), and its 90% confidence
996 bound calculated with an F-test (gray, dotted). (b) As in (a) but for Mindanao, averaged inside box M.

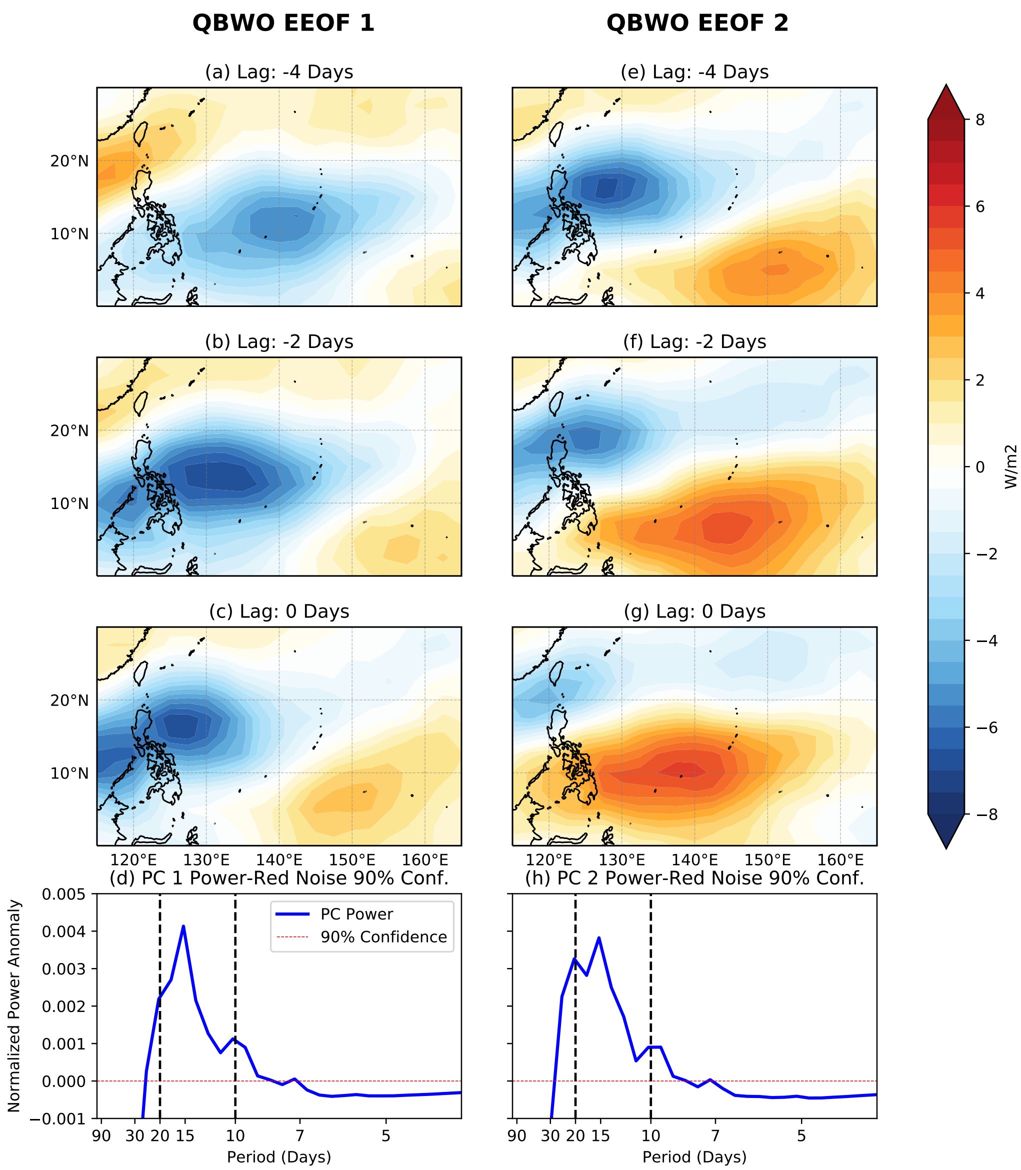

FIG. 3. Spatial pattern at -4 (top), -2 (middle), and 0-day (bottom) lags from extended EOFs 1 (left) and 2 (right) of 10-20 day bandpass filtered AVHRR OLR anomalies in physical units (W m^{-2}). The bottom row shows the difference between power spectra of each corresponding principal component time series and the corresponding 90% confidence bound of a theoretical red noise spectrum with the same autocorrelation as the PC time series. Values above zero (dotted red line) can be considered statistically significant at the 90% confidence level.

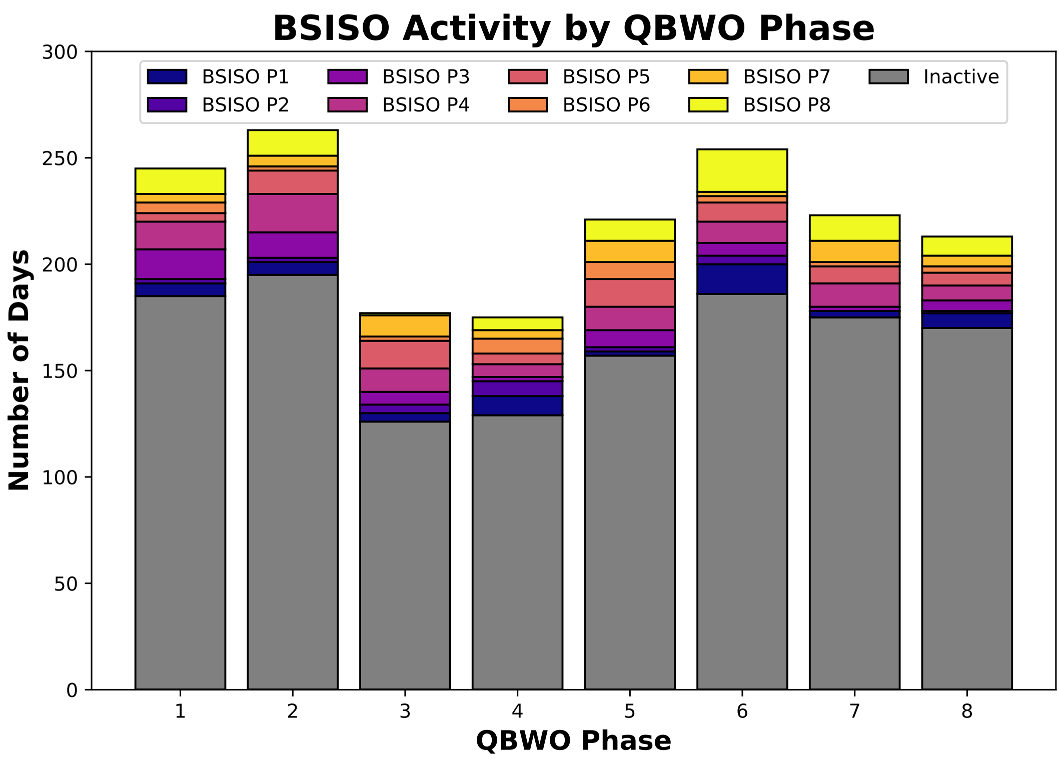

FIG. 4. Number of days in a certain Lee et al. (2013) BSISO phase distributed by active QBWO phase. The BSISO is considered to be inactive when the amplitude of the index is less than one. The darker color in the stacked bar chart indicates days that are classified as the same phase number in both indices.

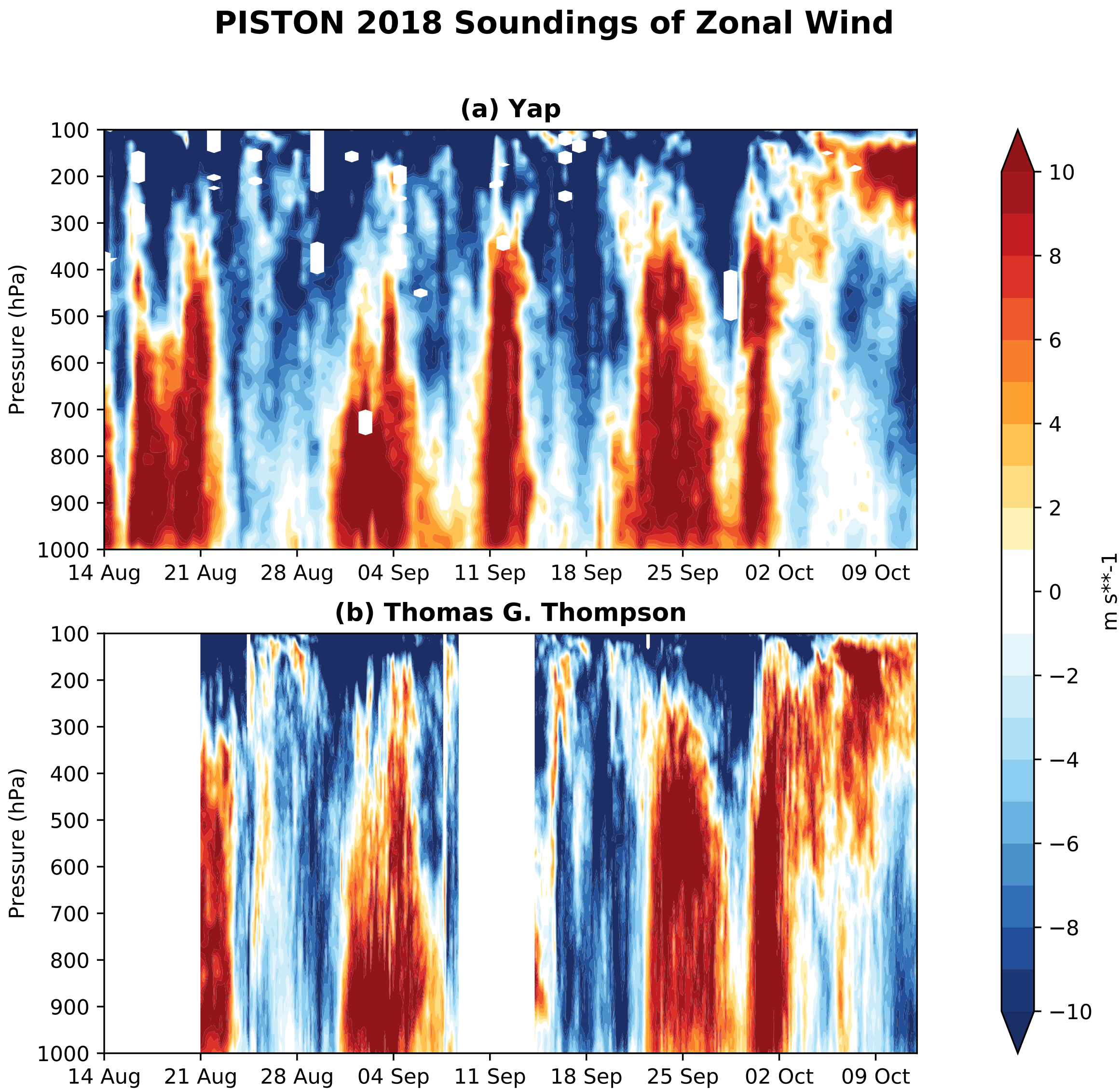

1005 FIG. 5. Time-height diagram of zonal wind from each sounding taken as part of the PISTON field campaign
1006 between 14 August 2018 and 13 October 2018. Soundings were taken every 12 hours from the island of Yap
1007 (top) and every 3 hours from the R/V Thomas G. Thompson during operational periods (bottom).

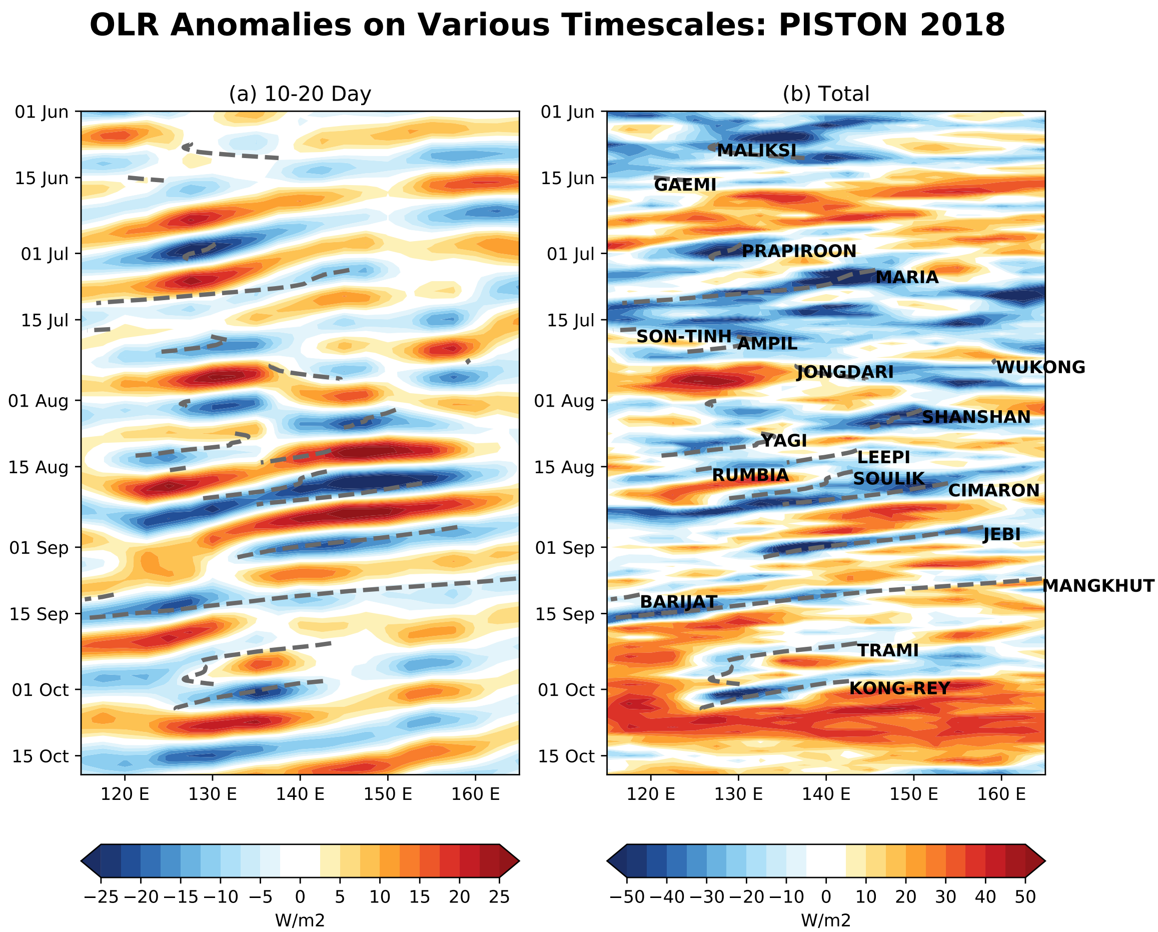

FIG. 6. Hovmöller plot of AVHRR OLR averaged between 0 and 25N at each longitude during 1 June-20 October 2018, bandpass filtered to the 10-20 day timescale using a Lanczos filter with 93 weights in W m^{-2} (left), and OLR anomalies from the seasonal cycle defined by the average daily climatology smoothed with a 7-day running mean (right). Named tropical cyclone tracks from IBTrACS are superimposed with gray dotted lines when the storm center was inside 0-25N.

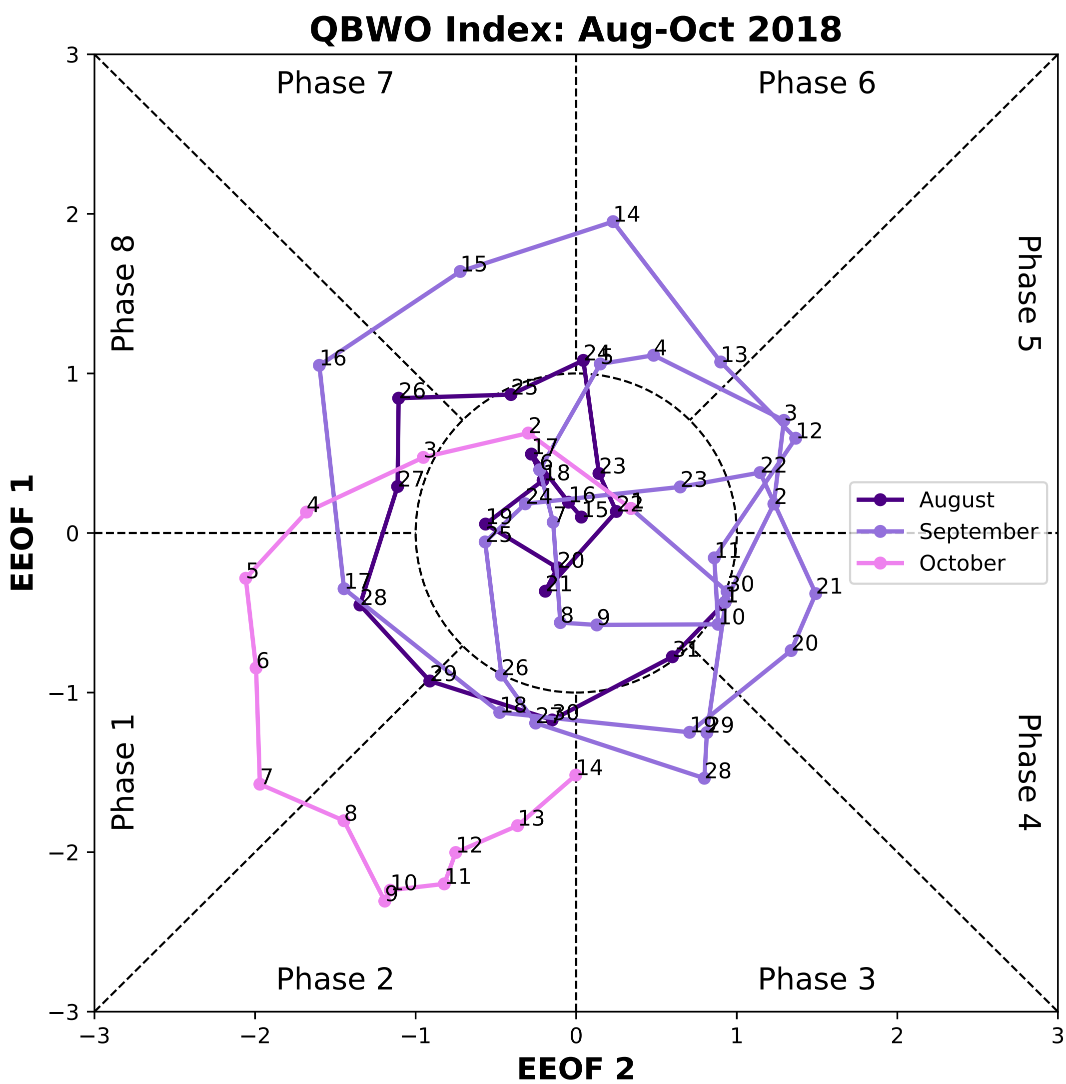

FIG. 7. Phase space diagram of the QBWO index activity from 14 August-14 October 2018 (the PISTON field campaign period), with the first principal component on the y-axis and the second principal component on the x-axis. The split between the 8 phases is denoted with black dotted lines, while days with an amplitude less than 1 (inside the center circle) are considered inactive, and not part of any phase. August is shown in the darkest color, with October in the lightest pink. The corresponding numbers indicate the date of each month.

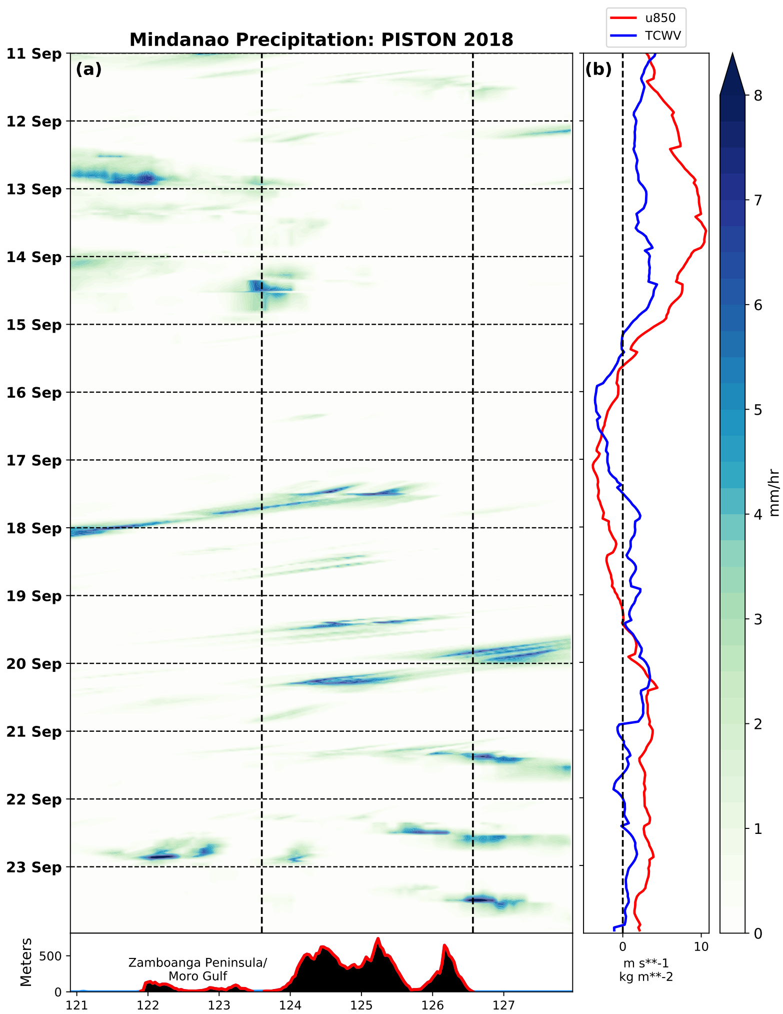

FIG. 8. (a) CMORPH precipitation rate estimates (mm/hr) averaged from 6N-8N across Mindanao (Box M, Fig. 1) from 11 September 2018 to 23 September 2018, during one full cycle of the QBWO index. The average topography in this box from NOAA ETOPO2 is shown on the bottom, with the coastlines drawn as vertical dashed black lines. Note that there are some land points west of the western coastline here, part of the Zamboanga Peninsula. The horizontal dashed black lines correspond to 00 UTC, or 0800 local time. (b) Zonal wind at 850-hPa averaged across both latitude and longitude in Box M (red line) and total column water vapor (blue line) from ERA5, with the JJAS composite diurnal cycle removed at each hour.

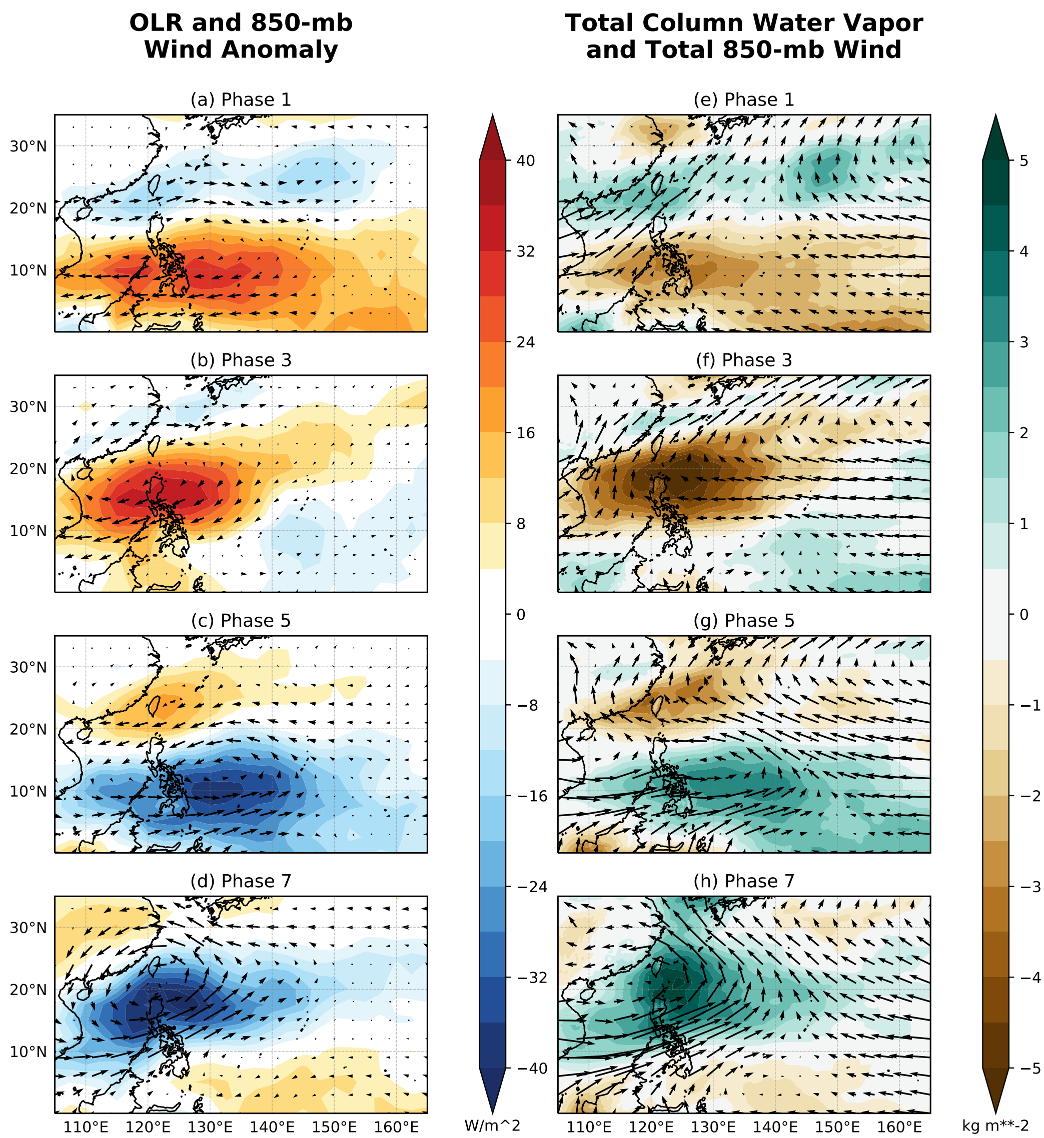

FIG. 9. Composite maps by select QBWO phase over the West Pacific ocean of anomalies of OLR (W m^{-2}) and vector anomalies of 850-mb wind from ERA5 (left column), and anomalies of ERA5 total column water vapor (kg m^{-2}) with total 850-mb vector wind (right column). The total number of days in each composite can be ascertained from Figure 4

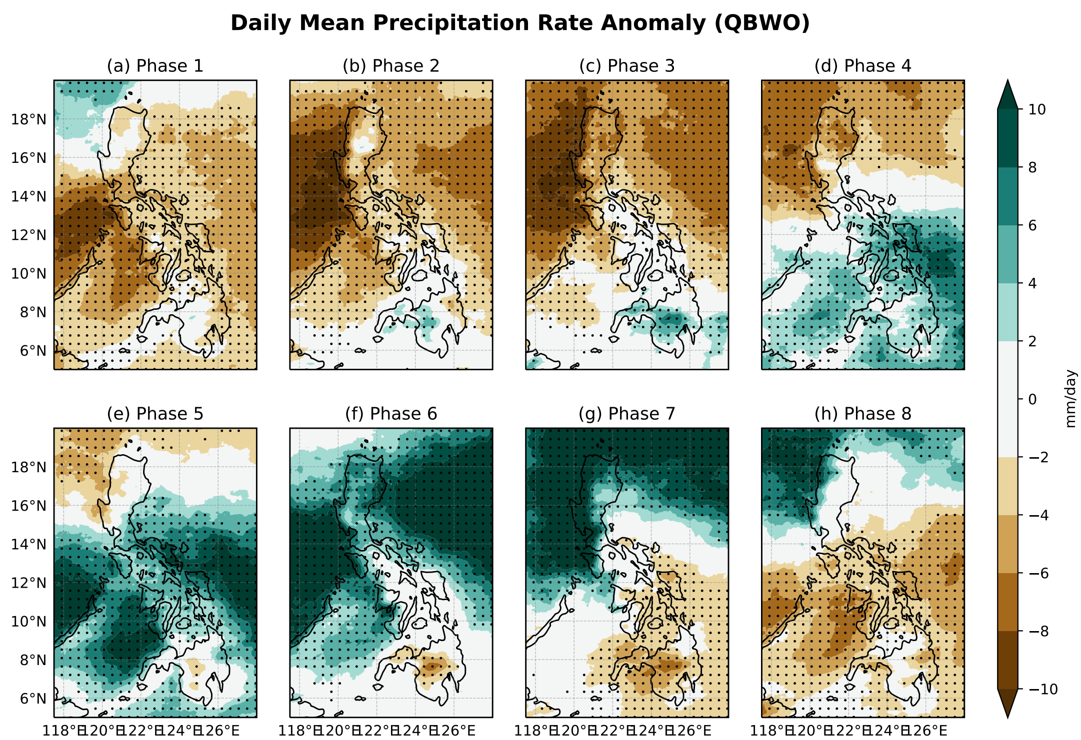

1029 Fig. 10. Anomalies in daily mean CMORPH precipitation rate composited by QBWO phase, with statistical significance at the 95% confidence level shown as dots.

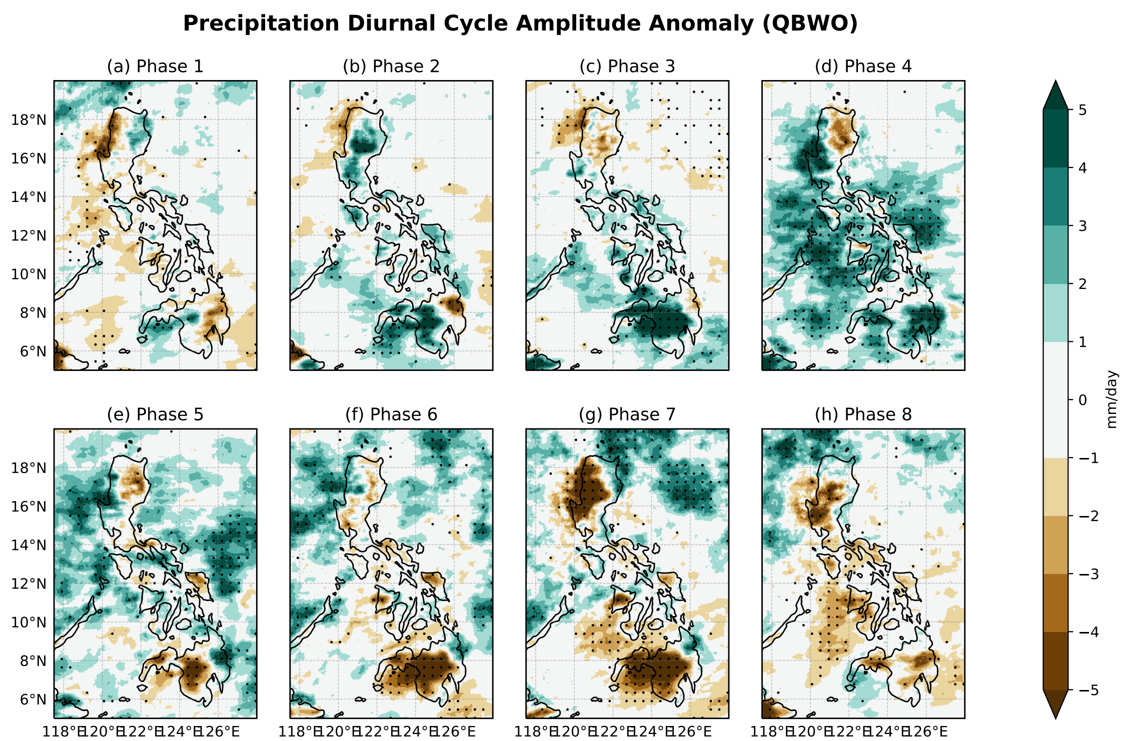

1031 FIG. 11. Anomalies in the amplitude of the CMORPH precipitation rate diurnal cycle by QBWO phase.
1032 Anomalies are calculated as the difference in diurnal amplitude between each phase composite, and amplitude
1033 of the JJAS composite diurnal cycle. Statistical significance at the 95% confidence level is shown as dots.

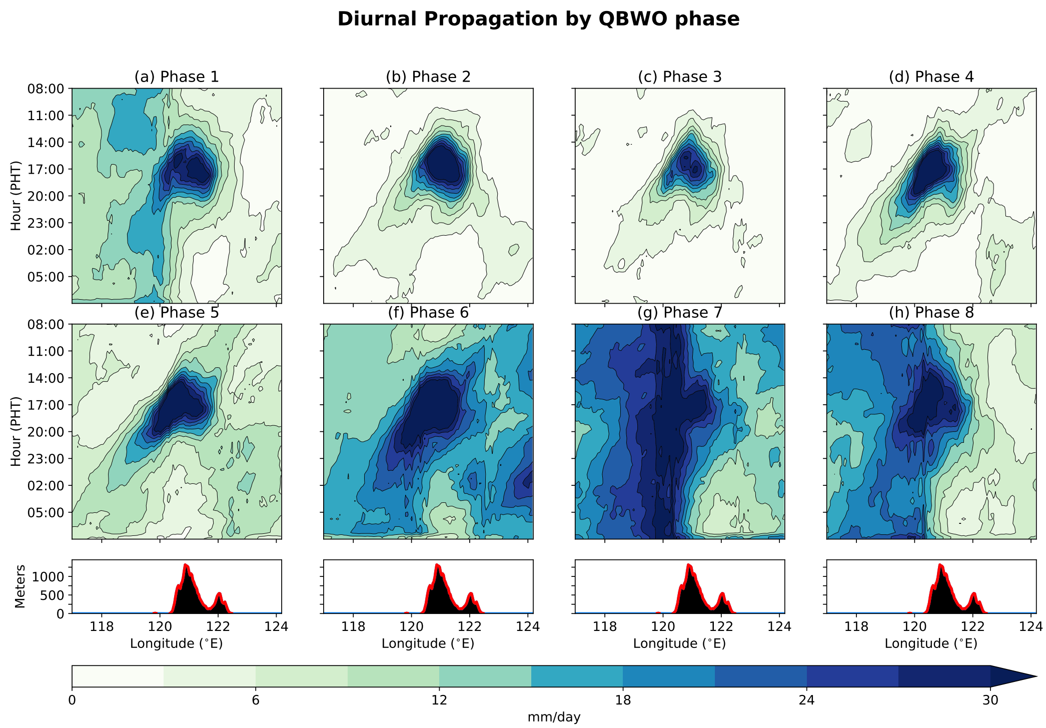

1034 FIG. 12. Hovmöller diagrams of the composite diurnal cycle of CMORPH precipitation rate (mm/day) for select phases of the QBWO index calculated by projecting unfiltered OLR anomalies onto the EEOF spatial patterns shown in Fig. 3 (top), and the index calculated by projecting 10-20 day bandpass filtered OLR anomalies onto the same EEOF patterns (bottom). Precipitation rates are averaged across latitude in box L (Fig. 1), with corresponding longitude noted below. The average elevation of topography from NOAA ETOPO2 inside box L is shown at the bottom for reference.

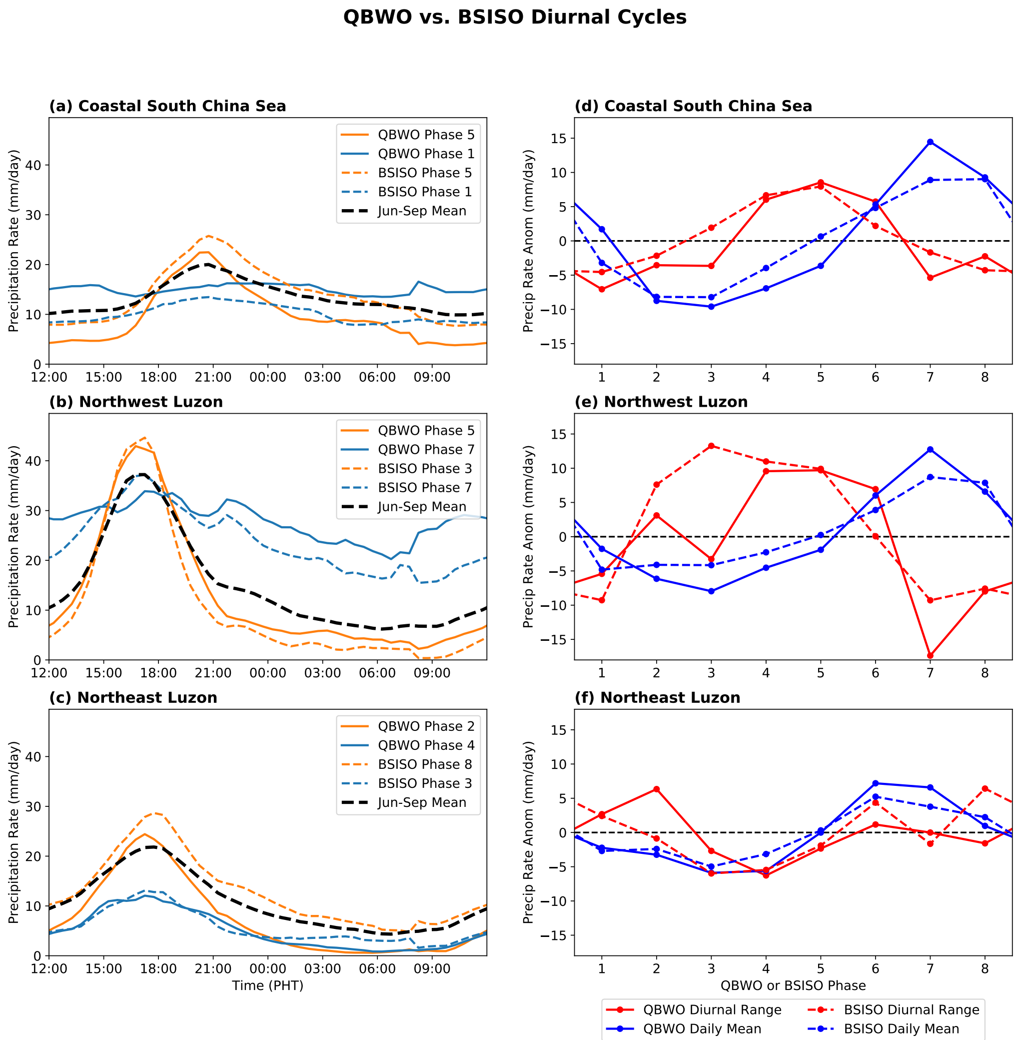

FIG. 13. (a-c) Composites of the spatially averaged diurnal cycle of CMORPH precipitation rate (mm/day) in the QBWO (solid) and Lee et al. (2013) BSISO (dotted) phase with the highest diurnal range (orange), the QBWO/BSISO phase with the smallest diurnal range (blue), and the full JJAS composite (dotted black). Spatial averaging is done over ocean points inside box A (a), and land points inside boxes B (b) and C (c). (d-f) The corresponding daily mean precipitation (blue) and diurnal range (red) in mm/day of each phase's spatially averaged composite diurnal cycle, by QBWO phase (solid) and BSISO phase (dotted). Each box covers a domain near Luzon.

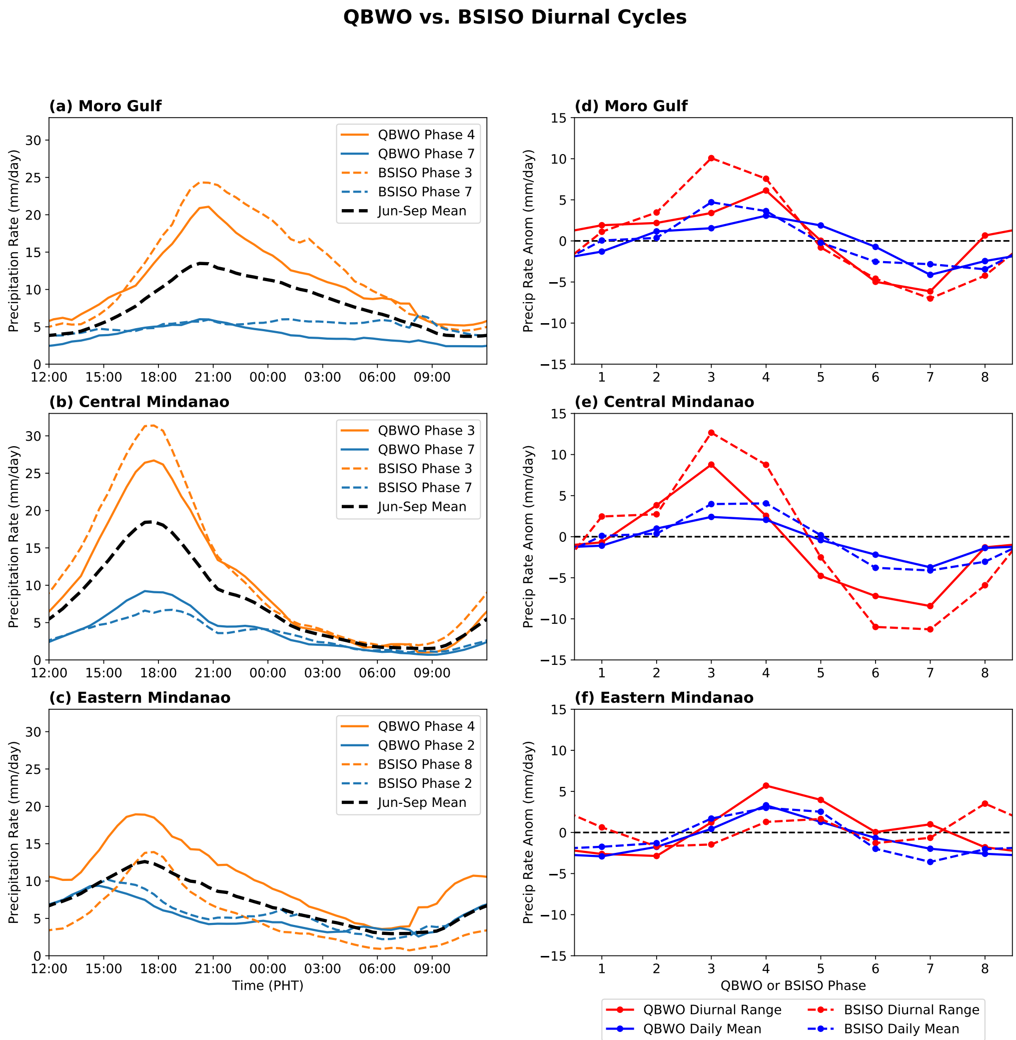

FIG. 14. (a-c) Composites of the spatially averaged diurnal cycle of CMORPH precipitation rate (mm/day) in the QBWO (solid) and Lee et al. (2013) BSISO (dotted) phase with the highest diurnal range (orange), the QBWO/BSISO phase with the smallest diurnal range (blue), and the full JJAS composite (dotted black). Spatial averaging is done over ocean points inside box D (a), and land points inside boxes E (b) and F (c). (d-f) The corresponding daily mean precipitation (blue) and diurnal range (red) in mm/day of each phase's spatially averaged composite diurnal cycle, by QBWO phase (solid) and BSISO phase (dotted). As in Fig. 13 but for Mindanao.

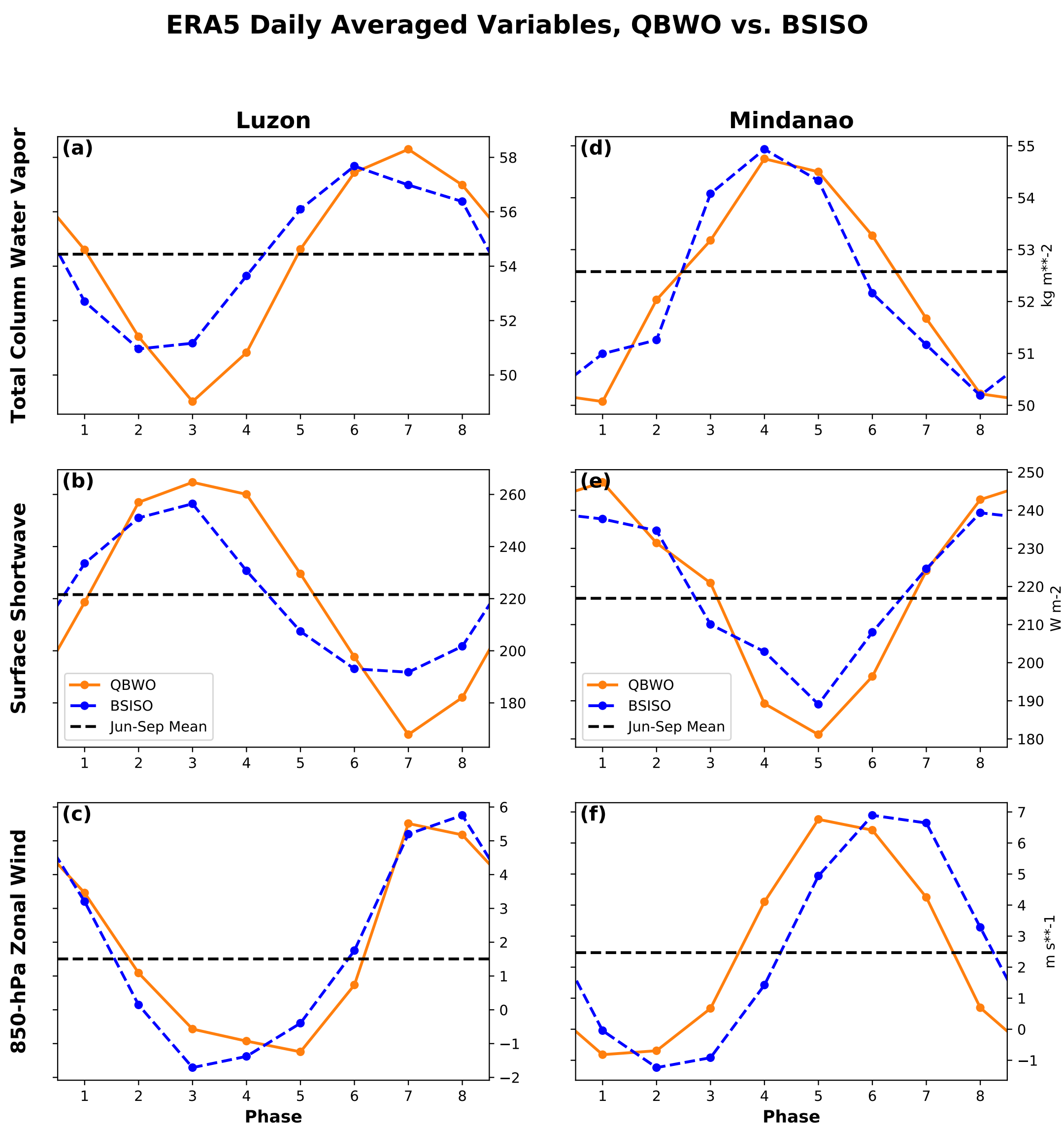

1054 FIG. 15. Daily mean values of select variables from ERA5 composited by QBWO phase (solid, orange) and
1055 BSISO phase (dotted, blue), averaged over box L covering Luzon (left) and box M covering Mindanao (right).
1056 Total column water vapor (kg m^{-2}) is shown on top (a, d), downwelling shortwave radiation (W m^{-2}) at the
1057 surface in the middle row (b, e), and 850-hPa zonal wind (m s^{-2}) at the bottom (c, f). Corresponding JJAS mean
1058 values for each variable on each island are shown as a horizontal dotted black line.

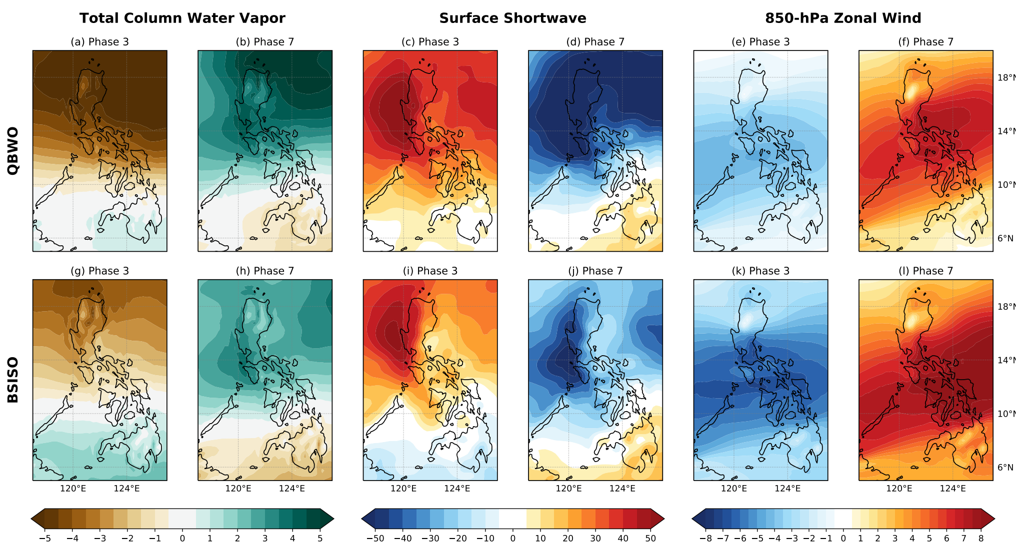

FIG. 16. Daily mean anomalies from JJAS average of select variables from ERA5 composited by QBWO phase (top) and BSISO phase (bottom) over the Philippines. For each variables, phase 3 of each index is shown at the left, and phase 7 at the right. The grouping of 4 panels at the left shows total column water vapor (kg m^{-2}), the middle grouping shows downwelling shortwave radiation (W m^{-2}) at the surface, and the right grouping shows 850-hPa zonal wind (m s^{-2}).